Review

Advanced semiconductor catalyst designs for the photocatalytic reduction of CO$_2$

Zhangsen Chen [a], Gaixia Zhang [b,**], Siyi Cao [c], Guozhu Chen [c], Cuncheng Li [c], Ricardo Izquierdo [b], Shuhui Sun [a,*]

[a] Institut National de la Recherche Scientifique – Centre Énergie Matériaux Télécommunications, Varennes, Québec, J3X 1P7, Canada
[b] Department of Electrical Engineering, École de Technologie Supérieure (ÉTS), Montréal, Québec, H3C 1K3, Canada
[c] School of Chemistry and Chemical Engineering, University of Jinan, Jinan, 250022, PR China

A B S T R A C T

Using clean solar energy to reduce CO$_2$ into value-added products not only consumes the over-emitted CO$_2$ that causes environmental problems, but also generates fuel chemicals to alleviate energy crises. The photocatalytic CO$_2$ reduction reaction (PCO$_2$RR) relies on the semiconductor photocatalysts that suffer from high recombination rate of the photo-generated carriers, low light harvesting capability, and low stability. This review explores the recent discoveries on the novel semiconductors for PCO$_2$RR, focusing on the rational catalyst design strategies (such as surface engineering, band engineering, hierarchical structure construction, single-atom catalysts, and biohybrid catalysts) that promote the catalytic performance of semiconductor catalysts on PCO$_2$RR. The advanced characterization techniques that contribute to understanding the intrinsic properties of the photocatalysts are also discussed. Lastly, the perspectives on future challenges and possible solutions for PCO$_2$RR are presented.

1. Introduction

Over the decades, the large consumption of fossil fuels due to anthropogenic activities has released heat and greenhouse gas into the atmosphere. The concentration of CO$_2$, one of the major greenhouse gases, in the atmosphere exceeds 410 parts per million (ppm), which is much higher than 280 ppm in the pre-industrial period.[1] The thermal radiation from the sunlight and the surface of the earth can be trapped by CO$_2$ molecules, augmenting the global temperature and aggravating the issue of global warming.[2] The over-emitted CO$_2$ is truly one of the top concerns for human society. The CO$_2$ reduction reactions (CO$_2$RR) that convert CO$_2$ molecules into value-added products such as CH$_3$OH, CH$_4$, CO, and HCOOH give an alternative strategy to consuming CO$_2$, while mitigating the energy crises. In addition, realizing CO$_2$RR by clean energies such as solar energy offers an approach to alleviate both global warming and energy crisis issues in a green concept.[3] To fulfill this,

photocatalytic CO$_2$ reduction reactions (PCO$_2$RR) has gained much attention because it utilizes semiconductor materials as photocatalysts to absorb sunlight as the driving force to reduce CO$_2$. Fig. 1a depicts the fundamentals of PCO$_2$RR on a semiconductor catalyst. Typically, the photocatalysis takes three main steps: i) the generation of the photo-generated carriers (e$^-$/h$^+$ pairs) within the semiconductor photocatalyst through harvesting the incident light; ii) the transfer of the photo-generated electrons and holes to the surface of the photocatalyst; iii) the catalytic reactions (CO$_2$RR and the oxidation half-reaction) on the surface of the photocatalyst.[4] The photo-generated carriers (e$^-$/h$^+$ paires) are essential to PCO$_2$RR, as they are the keys to the catalytic reactions. The photo-generated electrons in the conduction band (CB) participate in CO$_2$RR to reduce CO$_2$ molecules. The photo-generated holes in the valence band (VB) participate in the counter-reaction (oxidation half-reactions, such as water oxidation reaction). During the formation of the photo-generated carriers, the electrons and holes tend to

* Corresponding author.
** Corresponding author.
   E-mail addresses: gaixia.zhang@etsmtl.ca (G. Zhang), shuhui.sun@inrs.ca (S. Sun).
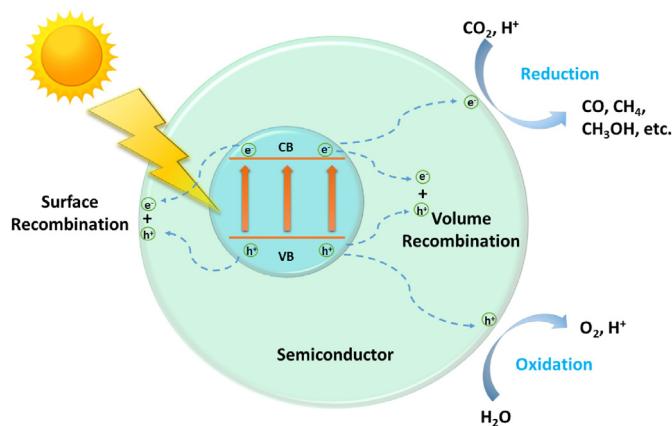
**Fig. 1.** Schematic of photocatalytic CO_2 reduction reactions (PCO_2RR). Reproduced with permission from Ref. 7.

Fig. 2. Advanced semiconductor catalysts for PCO_2RR.

recombine with each other through surface recombination and volume recombination, which prohibits catalytic efficiency. Besides, the potentials of the VB maximum and the CB minimum need to straddle the redox potentials of the oxidation half-reactions and CO_2RR, respectively.[5] Equations (1)–(8) shows some typical reaction steps involved in CO_2RR, along with the reactions for H_2 and O_2 productions (vs. Normal Hydrogen Electrode (NHE), in aqueous solution of pH = 7).[3,6]

$$CO_2 + e^- \rightarrow CO_2^{\bullet -} \quad E = -1.90 \text{ V} \tag{1}$$

$$CO_2 + 2H^+ + 2e^- \rightarrow HCO_2H \quad E = -0.61 \text{ V} \tag{2}$$

$$CO_2 + 2H^+ + 2e^- \rightarrow CO + H_2O \quad E = -0.53 \text{ V} \tag{3}$$

$$CO_2 + 4H^+ + 4e^- \rightarrow HCHO + H_2O \quad E = -0.48 \text{ V} \tag{4}$$

$$2H^+ + 2e^- \rightarrow H_2 \quad E = -0.42 \text{ V} \tag{5}$$

$$CO_2 + 6H^+ + 6e^- \rightarrow CH_3OH + H_2O \quad E = -0.38 \text{ V} \tag{6}$$

$$CO_2 + 8H^+ + 8e^- \rightarrow CH_4 + 2H_2O \quad E = -0.24 \text{ V} \tag{7}$$

$$2H_2O - 4e^- \rightarrow O_2 + 4H^+ \quad E = +0.82 \text{ V} \tag{8}$$
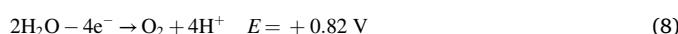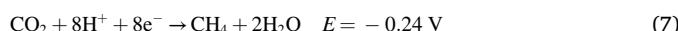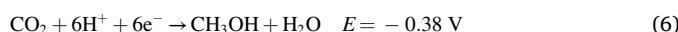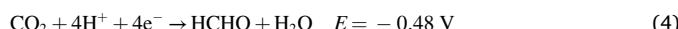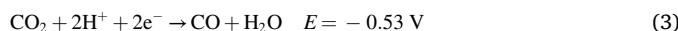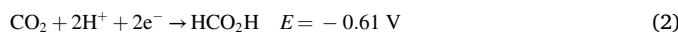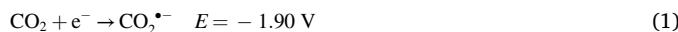
The semiconductor catalyst needs to meet not only the kinetic barriers but also the thermodynamic requirements to achieve a successful PCO_2RR. Moreover, the bandgap between CB and VB determines the wavelength range that the semiconductor can absorb from sunlight. When the value of the bandgap is larger than ca. 3.1 eV, the semiconductor catalyst can solely harvest ultra-violet illumination, which is only a small fraction of the sunlight. Increasing the light-harvesting ability of the photocatalysts requires the bandgap of the semiconductor materials to be relatively narrow. The single pure semiconductor catalyst alone usually cannot afford sufficient catalytic efficiency for PCO_2RR. Great efforts are made in the modification of the semiconductor catalysts (e.g. the refinement of crystallinity, defect engineering, heterojunction construction, etc.) to increase the catalytic performance (e.g. product selectivity and activity, light harvesting capability, stability) during PCO_2RR.[5] The goal is to design rational photocatalysts with: I) the matching CB and VB potentials for CO_2RR and the oxidation half-reactions; II) the narrow bandgap to absorb sufficient sunlight; III) low recombination rate of the photo-generated carries; IV) sufficient and highly efficient active sites for CO_2RR and the oxidation half-reactions. This review concentrates on the most recent advanced photocatalyst designs for PCO_2RR, where the superiorities of semiconductor modification and integration are highlighted (Fig. 2). Hybridization strategies of photocatalysts such as surface engineering and band engineering are explained with some typical examples (e.g. co-catalyst designs, photosensitizer, heterojunction construction). Then, promising results from structural engineering and single-atom active site fabrications are exposed, along with the biohybrid catalyst designs. Finally, the perspectives on the remaining challenges and future focuses are presented.
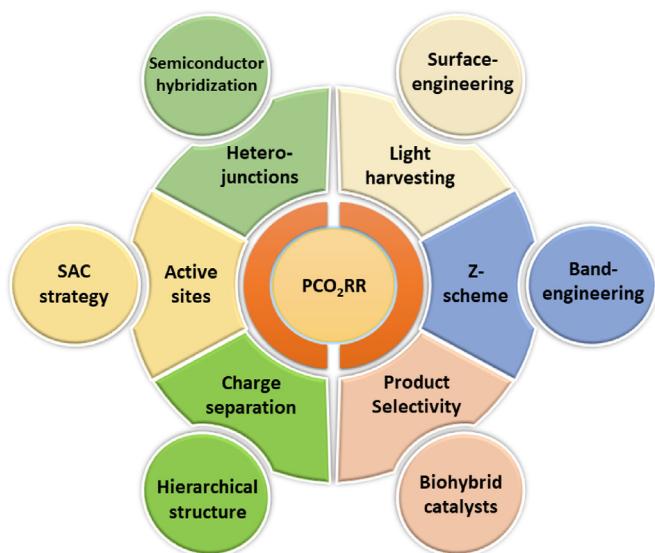
2. Hybridization of semiconductor catalysts for PCO_2RR

Currently, mainstream works focus on modifying the semiconductor photocatalysts by hybrid engineering such as surface modification and the integration of different semiconductors to form heterojunctions. Table 1 lists some typical hybrid photocatalysts for PCO_2RR.

2.1. Surface engineering

As the catalytic reaction takes place on the surface of the catalyst, its modification with active sites or support co-catalysts is a promising way to enhance the catalytic activities of the catalyst materials. For example, An et al. modified the Fe tetraphenyl porphyrin (FeTPP) catalyst with an alkyne-functionalized supramolecular synthon to form an iron porphyrin box (PB) bearing 24 cationic groups (FePB-2(P)) that offered a synergy of porosity and charge effects. The modified FePB-2(P) exhibited a 41-times enhancement in catalytic performance, as compared to the original FeTPP, toward CO production in PCO_2RR.[8] The modification of the metal co-catalysts on the semiconductor surface can serve as not only the active sites to capture CO_2 molecules for the activation but also the electron trap to separate photo-generated carriers, demonstrating excellent PCO_2RR performance (e.g, Au–Cu alloy modified on TiO_2 substrates for CH_4 and C_2H_4 productions[9]; Ni cluster shell on NiO core for the CO generation[10]).

Surface engineering for light harvesting enhancement is another approach to increase photocatalytic efficiency. As photocatalysis utilizes solar energy to drive the catalytic reactions, the photocatalysts' efficiency of harvesting sunlight is vital in the practical aspect. Currently, many good semiconductor catalysts such as metal oxides exhibit wide bandgap, which limits light absorption within the ultra-violet range, only a small fraction of the incident solar radiation (less than 5%).[11] It makes those wide-bandgap photocatalysts less attractive in industrial applications, as sunlight mostly contains visible and infrared lights. The integration of semiconductor catalysts with light-response-efficient materials allows for the improved light-harvesting ability of the photocatalysts. Modifying semiconductor catalyst surfaces with photosensitizers is one of the approaches to achieve this goal. Wang et al. constructed a number of

Table 1
Photocatalytic performance of some typical hybrid catalysts.

| Catalyst	Light source	Reduction product (selectivity)	Production rate (µmol g^{-1} h^{-1})	Stability	Other parameters	Ref.
Metal oxides						
CoO_x/N–C–ZnO	AM 1.5G light	CO	CO: 2.6	5 h	CO_2 + H_2O; Apparent quantum yield: 1.49% at 420 nm	71
NiO/hexaniobate-Ni cluster	Simulated solar light (150 W)	CO	CO: 730		CO_2 + H_2O	72
Ag–TiO_2/GDL	UV light (λ < 400 nm)	CO (~66%), CH_4 (~33%)	CO + CH_4: 305.7	60 h	CO_2 + H_2O	23
CeO_2@CeO_2/TiO_2	AM 1.5G light	CO (~87%), CH_4 (~13%)	CO: 97.6 CH_4: 15.0	8 h	CO_2 + H_2O and triethanolamine (TEOA)	40
$Au_{0.2}Cu_{0.8}$/TiO_2	AM 1.5G light	CH_4 (~90%), C_2H_4 (~10%)	CH_4: 3578.9 CH_4: 369.8	8 h	CO_2 + H_2O	9
Pd-HPP-TiO_2	300 W Xe lamp	CO (~41%), CH_4 (~59%)	CO: 34.0 CH_4: 48.0	20 h	CO_2/O_2 mixed gas, or air	22
Cu_2O-111-Cu^0	300 W Xe lamp	CH_4 (~97%), C_2H_4, CO, H_2	CH_4: 78.4	8 h	CO_2 + H_2O	73
Alloys						
Au/CuPd	400 mW cm^{-2} full-spectrum light	CH_4 (100%)	CH_4: 15.6	30	CO_2 + H_2O Apparent quantum efficiency: 0.38% at 800 nm	28
Bi-based						
BiOCl–V_{Bi}	300 W Xe lamp	CO	CO: 21.99	30 h	In air	74
Ni@MOF/$BiVO_4$	300 W Xe lamp	CO (99.2%), H_2	CO: 178.0	28 h	CO_2 + H_2O	75
$SrTiO_3$:La,Rh/Au/$BiVO_4$:Mo	AM 1.5G light	$HCOO^-$ (97%)	$HCOO^-$: ~20.0	24 h	CO_2-saturated 0.1 M $KHCO_3$ aqueous solution + CO_2; Turnover number (TON): 427	34
CdS-based						
α-Fe_2O_3/CdS	AM 1.5G light	CO	CO: 9.3	6 h	CO_2 + H_2O	33
$ZnIn_2S_4$–CdS	visible light (λ > 420 nm)	CO (~85%), H_2	CO: 2182.5	20 h	CO_2 + H_2O, TEOA, MeCN, $CoCl_2$, and 2,2-bipyridine; TON = 43.65	31
Layered double hydroxides						
NiAl-LDH	visible light (λ > 600 nm)	CO (29.7%), CH_4 (70.3%)	CO: 43.0 CH_4: 103.0	4 h	CO_2 + H_2O, acetonitrile (ACN), TEOA, and $Ru(bpy)_3Cl_2$·$6H_2O$;	20
Pd/CoAl-LDH	visible light (λ > 400 nm)	CO (50%), H_2 (50%)	CO: 1680.0	4 h	CO_2 + H_2O, TEOA, and $Ru(bpy)_3Cl_2$· $6H_2O$;	21
Carbonaceous						
CN/MRF	visible light (λ > 420 nm)	CH_3OH	CH_3OH: 0.99	5 h	CO_2 + H_2O, 80 °C; Quantum efficiency: 5.5% at 380 nm	76
Co_2P@BP/g-C_3N_4	300 W Xe lamp	CO (96%), CH_4	CO: 16.21	20 h	CO_2 + acetonitrile, H_2O, and TEOA	77
Cu_1N_3@PCN	visible light (λ > 420 nm)	CO	CO: 49.8	25 h	CO_2 + H_2O	78
Fe SA/COF	visible light (λ > 420 nm)	CO (96.4%), H_2	CO: 980.3	20 h	CO_2 + acetonitrile, H_2O, and TEOA	79
HOF–Ni/GO	visible light (λ > 420 nm)	CO (96.3%), H_2	CO: 24323.0	8 h	CO_2 + H_2O, MeCN, TIPA, and $Ru(bpy)_3Cl_2$· $6H_2O$;	80
Au/N-graphene	300 W Xe lamp	CO (95%)	CO: 111360	36 h	CO_2 + H_2O	51
Perovskite						
$Cs_2NaBiCl_6$	300 W Xe lamp	CO (96.4%), CH_4 (3.6%)	CO: 30.22 CH_4: 1.12	50 h	Gas (CO_2 + H_2O)	81
Ni–$CsPbBr_3$/Bi_3O_4Br	visible light (λ > 420 nm)	CO (98.2%), CH_4 (1.8%)	CO: 96.9 CH_4: 1.7	20 h	Gas (air + H_2O)	32

photosensitizers of homoleptic Al (III) for PCO_2RR with emission quantum yields from 10% to 40%.[12] Fig. 3a shows the molecular structures of the homoleptic Al (III) complexes. The light absorption band center can be tuned by changing the ligands attached to the Al (III) photosensitizers (Fig. 3b). Fig. 3d illustrates the PCO_2RR activities of different catalysts coupled with Al (III) photosensitizers. The catalyst of [Fe(qpy)(OH₂)₂](ClO₄)₂ (FeQPY; qpy = 2,2′:6′,2″:6″,2‴-quaterpyridine) affords the most durable and stable CO production among all the catalysts. Fig. 3c demonstrates the reaction scheme for the PCO_2RR with Al (III) photosensitizers/FeQPY with 1,3-dimethyl-2-phenyl-2,3-dihydro-1H--benzo[d]-imidazole (BIH) as the sacrificial electron donor. This noble-metal-free system achieves a CO selectivity of 99% and a TON value of 10250 under 450 nm light illumination in PCO_2RR (Fig. 3e). Das et al. developed a porous organic polymer (POP) as a light harvester for improving PCO_2RR. The composite catalyst of $In_{2.77}S_4$ and POP was built by electrostatic interaction and exhibited a C_2H_4 product selectivity of 98.9% with a yield rate of 67.65 µmol g^{-1} h^{-1} under irradiation of visible light.[13]

To maximize the utilization of sunlight, scientists have discovered some promising semiconductor photocatalysts with narrow bandgap to harvest visible light, such as carbon nitride,[14–16] bismuth oxyhalides,[17,18] CdS,[19] layered double hydroxides (LDHs),[4,20,21] etc. However, those visible light-response semiconductor materials suffer from severe recombination of the photo-generated carriers. The surface modification

of the semiconductor catalyst with a metal co-catalyst such as Pd/TiO_2[22] and Ag–TiO_2,[23] which can trap the photo-generated electron, emerges as a powerful strategy to separate the photo-generated carries and contributes to for an enhanced PCO_2RR performance. It is well applied to visible light-response photocatalysts as well. For instance, Yue et al. reported a Bi-MOF/BiOBr photocatalyst where Bi-MOF was in-situ mounted on the BiOBr for PCO_2RR with a CO yield rate of 21.96 µmol g^{-1} h^{-1}.[24]

Another approach is to integrate the semiconductor catalysts with metal co-catalysts. In this strategy, using plasmonic metals offer extra benefits for light harvesting. The nanocatalysts of plasmonic metal interact strongly with incident light, generating a localized surface plasmon resonance (LSPR). The LSPR effect can easily tune the light absorption wavelength from ultra-violet to near-infrared through adjusting the geometry structure of the plasmonic metal catalyst.[25,26] For example, Cu/TiO_2 enables absorbance at 500–600 nm from the LSPR of Cu particles to improve the CO production in PCO_2RR.[27] The LSPR effect of Au particles helps achieving the PCO_2RR under low-intensity irradiation at 420 nm.[26]

Based on the promising results provided by the assistance of the plasmonic metal Au in light harvesting and catalytic performance, modifying Au catalyst with other metal alloys has proven to enhance the employment of photons with low energy for PCO_2RR. Hu et al. fabricated plasmonic light harvesting Au rods and coupled them with a co-catalyst

Fig. 3. (a) Synthetic diagram and molecular structures of different ligands applied for Al(III) PSs. (b) UV–vis absorption spectra and the normalized emission (λ_{exc} = 355 nm) spectra of **Al-4** (red), **Al-3** (orange), **Al-2** (gold), and **Al-1** (lime) in purified CH$_3$CN solution at 293 K. (c) Simplified reaction and energy scheme for visible-light-induced CO production in PCO$_2$RR by Al(III)-PSs/**FeQPY** with BIH as sacrificial electron donor. Product yields of CO (star) and H$_2$ (circle) under irradiations of (d) 405 nm and (e) 450 nm with 0.05 mM **FeQPY** and 0.5 mM PS in CO$_2$-saturated, 0.3 M TEOA CH$_3$CN, and 50 mM BIH solutions. Reproduced with permission from Ref. 12.

shell of CuPd alloy to achieve highly effective PCO$_2$RR to CH$_4$ production.[28] Fig. 4a demonstrates the structure of the Au/CuPd core-shell composite. Plasmonic catalysis often happens close to the surface of the catalyst (within the range of plasmon-induced local field). Pure Au nanorods are unlikely to collide with CO$_2$ molecules, resulting in its low CO$_2$ conversion efficiency (Fig. 4a, left). For Au/CuPd, the CuPd shell can capture CO$_2$ molecules to increase the CO$_2$ concentration on the surface of the catalyst, promoting the probability of further conversion and activation (Fig. 4a, right). The thickness of the shell and the Cu/Pd ratio can be easily adjusted by controlling the number of metal precursors during the synthesis. The optimized Au/CuPd catalyst can achieve a CH$_4$ yield rate of 15.6 μmol g^{-1} h^{-1}, which is almost 40 times higher than the one achieved by pure Au rods (Fig. 4b). The apparent quantum efficiency is up to 0.1% at 800 nm (Fig. 4d). The optimized thickness of the CuPd shell is believed to maximize the number of active sites on the catalyst surface and strengthen the electron-phonon scattering effect, contributing to the best CH$_4$ production. Fig. 4c illustrates that C$_2$H$_4$ and C$_2$H$_6$ can also be detected after the long-term reaction test. This suggests the multiple proton-coupled electron transfer ability of the Au/CuPd core-shell catalyst. To avoid the scattering loss of incident light during PCO$_2$RR, a spherical-structured gas-solid reaction system is further applied (Fig. 4e). The novel spherical-structured reaction system can realize the re-incidence of scattered photons, which benefits the catalytic

reaction system with a plasmonic effect. With the optimization of the partial pressure of CO$_2$ and the volume of H$_2$O in the system, the production rate of CH$_4$ can be further improved to 0.55 mmol g^{-1} h^{-1} (Fig. 4f). The spherical-structured reaction system affords a catalytic performance of around 35-folds to that of the conventional reaction system which only allows one single incident photon pass. Besides, the apparent quantum efficiency in the spherical-structured reaction system reaches 0.38% at 800 nm. It offers the opportunity to utilize the Au/CuPd core-shell catalyst in PCO$_2$RR under low-energy near-infrared irradiation.

2.2. Band engineering

When applied in photocatalysis, single pure semiconductors often suffer from the issues of wide bandgap that limits the visible light harvesting, unmatched CB or VB potential positions to drive the catalytic reactions, etc. Integrating two semiconductors with different CB and VB potential positions to form a heterojunction becomes a useful approach to overcome these difficulties.

There are three types of heterojunctions when integrating two different semiconductors. Type I is "straddling" where the CB and VB of one semiconductor are entirely contained in those of another semiconductor (Fig. 5a). In this type of heterojunction, both photo-generated
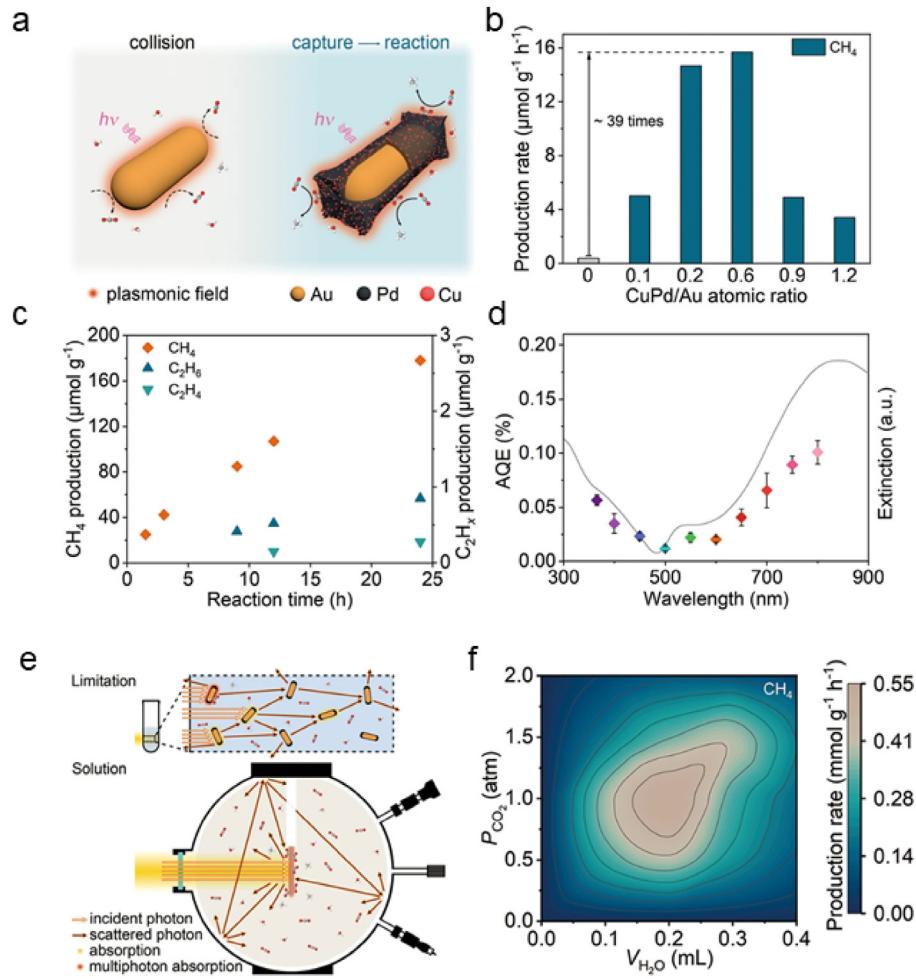
Fig. 4. (a) Schematic of CO_2 molecules being captured on the CuPd shell. (b) CH_4 production rates of Au/$CuPd_2$ with different thicknesses of the CuPd shell. (c) Time-dependent yield of CH_4 on Au/$CuPd_2$. (d) Calculated AQEs (dots) on Au/$CuPd_2$ under light illuminations with different monochromatic wavenumbers, compared to the UV–vis extinction spectrum (line). (e) Schematic of the gas-solid reaction, where full-spectrum light illuminates a spherical reactor. During catalysis, the scattered photons are reflected on the surface of the catalyst, which leads to multi-absorption processes for efficient PCO_2RR. (f) CH_4 yield rates through plasmon-induced PCO_2RR in the gas-solid reactor on Au/$CuPd_2$ under different H_2O volumes and CO_2 pressures. Reproduced with permission from Ref. 28.
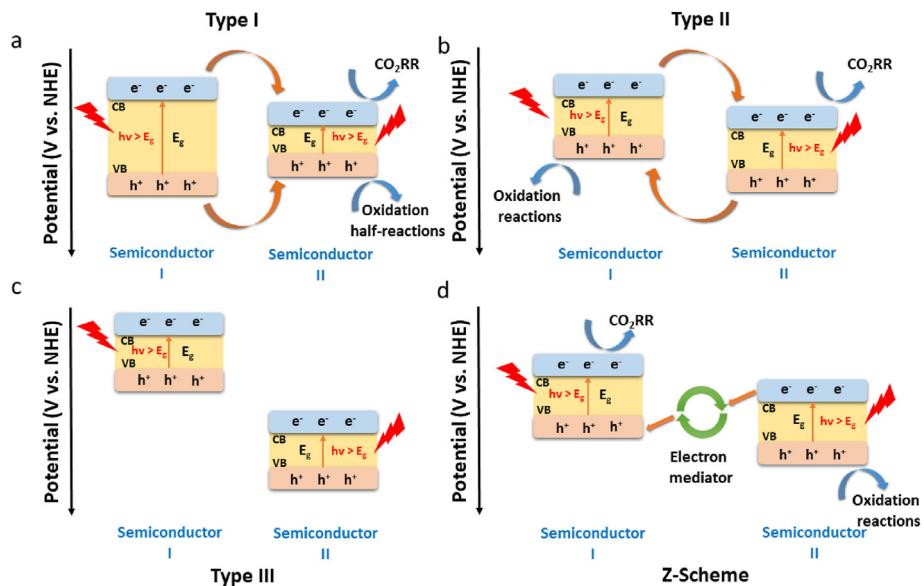
Fig. 5. Schematic of the band diagram on a semiconductor photocatalyst for CO_2RR and oxidation half-reactions: (a) Type I: straddling, (b) Type II: staggered, (c) Type III: broken gap, (d) Z-scheme. VB: valence band; CB: conduction band; h^+: hole; e^-: electron.

electrons in CB and holes in VB of semiconductor I tend to transfer to the CB and VB of semiconductor II by the potential difference, respectively. It comes with two drawbacks. First, the CB and VB potentials of

semiconductor II are less powerful to drive the catalytic redox reactions. Second, the accumulated photo-generated holes and electrons in semiconductor II exacerbate the recombination of the photo-generated

carriers. Hence, the "straddling type" heterojunction is not ideal for photocatalysis.

Type II is "staggered" where the CB and VB of one semiconductor overlap with those of another semiconductor (Fig. 5b), generating a favourable heterojunction. Once semiconductor I have more negative CB and VB potential positions than semiconductor II, the photo-generated electrons tend to transfer from the CB of semiconductor I to the CB of semiconductor II, while photo-induced holes tend to transfer from the VB of semiconductor II to the VB of semiconductor I. This new possible transfer pathway created by the "staggered type" heterojunction can separate the photo-generated electrons and holes in the semiconductors and significantly reduce the recombination rate of the photo-induced carriers in both semiconductor I and semiconductor II, boosting photocatalytic performance. The only drawback of this type of heterojunction is that the CB and VB that participate in the catalytic reactions are the less effective ones. Namely, the CB potential of semiconductor II is less negative than that of semiconductor I, and the VB of semiconductor I is less positive than that of semiconductor II.

Type III is a "broken gap" where the bandgaps of two semiconductors do not overlap (Fig. 5c). In this circumstance, the photo-generated electrons and holes between two semiconductors fail to transfer.[29] Therefore, the type II heterojunction is of interest in photocatalysis. Many works focus on the fabrication of type II heterojunction to boost catalytic performance. For example, a heterojunction between $CsPbBr_3$ and graphitic carbon nitride (g-C_3N_4) is built based on the band position differences between g-C_3N_4 and $CsPbBr_3$. It provides a stable CO yield rate of 975.57 $\mu mol \, g^{-1} \, h^{-1}$ in PCO_2RR for 76 h.[30] Zhu et al. constructed the heterojunction in a heterostructure of $ZnIn_2S_4$–CdS for PCO_2RR.[31] The ultrafast transient absorption spectroscopy proves the accelerated charge transport in the heterostructure (Fig. 6a and b). With the assistance of $Co(bpy)_3^{2+}$ as co-catalyst for CO_2RR and TEOA as the sacrificial compound to consume photo-generated holes (Fig. 6e), it exhibits the CO yield of around 33 μmol in the first hour (Fig. 6c) under visible light irradiation and retains its initial catalytic activity after 5 cycles (Fig. 6d) of the PCO_2RR measurements.

As aforementioned, the type II heterojunction still shows limits concerning the CB and VB positions that participate in the catalytic reactions. Inspired by natural photosynthesis, an electron transfer pathway where the photo-induced electron in the CB of semiconductor II travels to the VB of semiconductor I to perform the recombination is proposed

(Fig. 5d). It creates an electron transfer pathway with the shape of the letter Z, which is named "Z-scheme" in the heterojunction construction. The Z-scheme electron transfer pathway allows photo-generated carriers from the stronger CB and VB in the two semiconductors to participate in the catalytic reactions, which overcomes the difficulty raised in the type II heterojunction catalysts.

In another approach, the Z-scheme is constructed without building any additional bridge between two semiconductors, this is called the direct Z-scheme system.[6] The construction of the internal electric field in the heterojunction between two semiconductors proves to be an effective strategy to achieve the direct Z-scheme. Wang et al. built a 2D/2D Z-scheme heterostructure of Ni–$CsPbBr_3$/Bi_3O_4Br for PCO_2RR.[32] Driven by the difference in the Fermi levels of the two semiconductors, the photo-generated electrons transfer from Ni–$CsPbBr_3$ to Bi_3O_4Br. It leads to increased charge densities at the interface, positive on the Ni–$CsPbBr_3$ side and negative on the Bi_3O_4Br side, respectively. The internal electric field formed in this space charge region creates the band-bending effect. Fig. 7a depicts the Z-scheme electron transfer pathway where the electrons are directed from the CB of Bi_3O_4Br to the VB of Ni–$CsPbBr_3$. Because of the bending effect, the shape of the electron pathway looks more like the letter "S" rather than "Z". Under this circumstance, the term "S-scheme" is preferred over "Z-scheme" to highlight the band-bending effect. The Ni–$CsPbBr_3$/Bi_3O_4Br with the S-scheme heterostructure demonstrates an excellent 98.2% CO selectivity with a CO yield of 387.57 $\mu mol \, g^{-1}$, which is more than 10 times higher than that of $CsPbBr_3$ (Fig. 7b). Long et al. combined Fe_2O_3 and CdS to achieve the direct Z-scheme charge transfer pathway by a built-in internal electric field as well. The Z-scheme heterojunction of Fe_2O_3/CdS enables a CO yield of 9.3 $\mu mol \, g^{-1}$ in the first hour during PCO_2RR, which is much better than the sum of those of pure Fe_2O_3 and CdS.[33] The unique Z-scheme favors not only the separation of photo-generated electron-/hole pairs but also the redox capacity of the photo-generated electrons and holes involved in catalytic reactions such as CO_2RR.

Alternatively, when the Z-scheme is constructed with the help of the additional bridge between two semiconductors, it is called the indirect Z-scheme system. For example, Wang et al. delicately fabricated lanthanum (La)- and rhodium (Rh)-doped $SrTiO_3$ ($SrTiO_3$:La, Rh), the light absorber of Co(II) bis(terpyridine) modified molybdenum (Mo)-doped $BiVO_4$ ($BiVO_4$:Mo) and the RuO_2 catalysts on a gold layer ($SrTiO_3$:La, Rh|Au|RuO_2–$BiVO_4$:Mo) for the PCO_2RR (Fig. 7c). The Au layer in $SrTiO_3$:La,
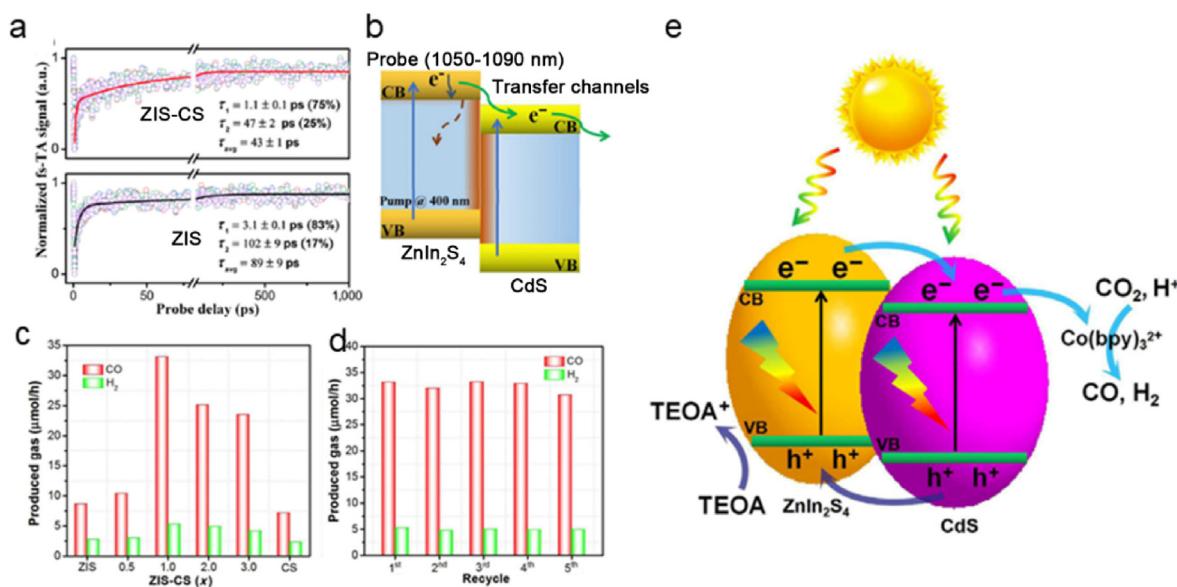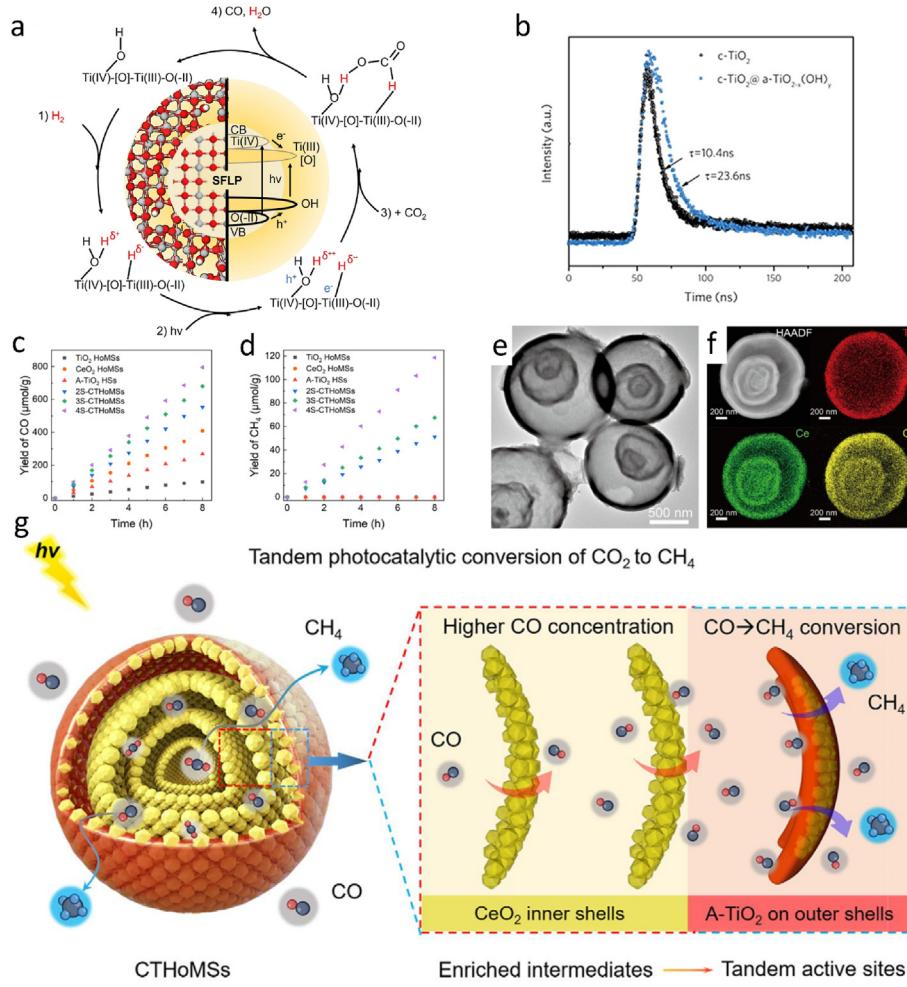

Fig. 6. (a) Global fitting and the ultrafast kinetics results (probing range: 1050–1090 nm with a 10 nm interval) for $ZnIn_2S_4$, and CdS QDs/$ZnIn_2S_4$. (b) Heterojunction schematic of $ZnIn_2S_4$–CdS. (c) PCO_2RR activities for $ZnIn_2S_4$, $ZnIn_2S_4$–CdS, and CdS. (d) Time-dependent PCO_2RR performance on $ZnIn_2S_4$–CdS. (e) Possible charge carrier transfer mechanism of $ZnIn_2S_4$–CdS for PCO_2RR under the irradiation of visible light. Reproduced with permission from Ref. 31.
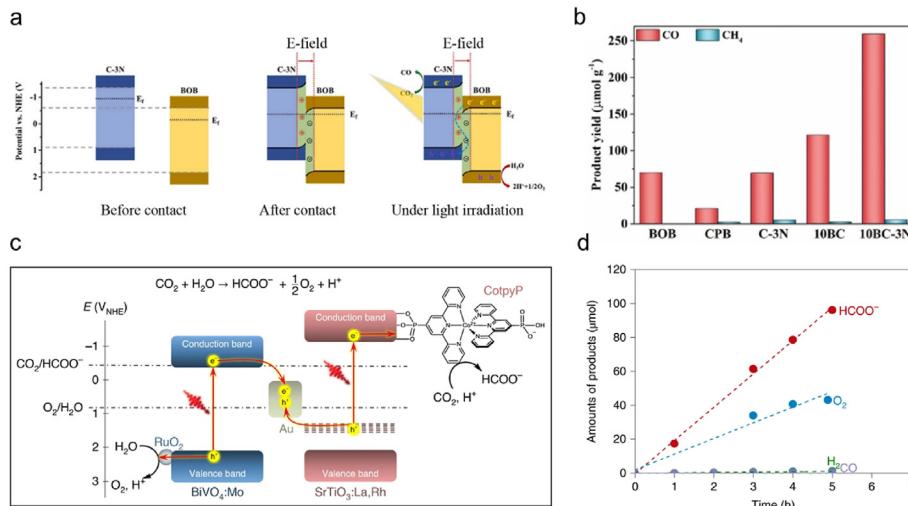
Fig. 7. (a) Schematic (individual, after contact, under the irradiation for CO$_2$RR with Z-scheme) of the band structures and the charge transfer pathways of C–3N and Bi$_3$O$_4$Br (BOB). (b) CO and CH$_4$ yield amount of C–3N, Bi$_3$O$_4$Br, and heterostructured catalysts. Reproduced with permission from Ref. 32. (c) Energy diagram of PCO$_2$RR coupled with water oxidation over SrTiO$_3$:La, Rh|Au|RuO$_2$–BiVO$_4$:Mo. The reduction potentials are given versus the NHE at pH 6.7. (d) Time course of the PCO$_2$RR and water oxidation over SrTiO$_3$:La, Rh|Au|RuO$_2$–BiVO$_4$:Mo. The reaction conditions: CO$_2$-saturated 0.1 M KHCO$_3$ aqueous solution, at 298 K. Reproduced with permission from Ref. 34.

Rh|Au|RuO$_2$–BiVO$_4$:Mo is believed to bridge the CB of RuO$_2$–BiVO$_4$:Mo and the VB of SrTiO$_3$:La, Rh, which constructs an effective indirect Z-scheme for the PCO$_2$RR to HCOO$^-$ and the H$_2$O oxidation reaction. It affords an HCOO$^-$ selectivity of 97% with a production rate of around 20 μmol g^{-1} h^{-1} (Fig. 7d).[34]

3. Hierarchical structure construction of the catalysts for PCO$_2$RR

The catalyst structure plays an essential role during photocatalysis, benefiting the spatial separation of the photo-generated carriers for improved catalytic performance. Taking 2D catalysts as an example, the

Fig. 8. (a) Illustration of the physicochemical properties of CO$_2$-to-CO by SFLPs in c-TiO$_2$@a-TiO$_{2-x}$(OH)$_y$. (b) Time-resolved photoluminescence spectroscopy decay curves of c-TiO$_2$ and c-TiO$_2$@a-TiO$_{2-x}$(OH)$_y$. Reproduced with permission from Ref. 39. (c) CO yield and (d) the CH$_4$ yield of the corresponding samples under AM 1.5 G illumination for 8 h. (e) HAADF-STEM images and (f) EDS mapping images of quadruple-shelled CeO$_2$@CeO$_2$/TiO$_2$. (g) Schematic of the hetero-shell structure and the tandem PCO$_2$RR to CH$_4$ in CeO$_2$@CeO$_2$/TiO$_2$. Reproduced with permission from Ref. 40.

ultra-thin 2D nanosheets facilitate the transfer of the photo-generated electron/hole pairs to the surface of the catalyst, promoting catalytic activity. For instance, ultrathin 2D NiMgV-layered double hydroxide nanosheets afford excellent CO and CH_4 productions in PCO_2RR.[35] Liang et al. constructed a 2D dislocated bilayer MOF that allowed 100% product selectivity of CO in PCO_2RR.[36] However, 2D structured materials often suffer from agglomeration, leading to the prolongation of the carriers' transfer and a decreased active area of the catalysts, which jeopardizes the catalytic performance. Wang et al. morphologically modified CuInZnS by introducing negatively charged $Ti_3C_2T_x$ to interfere with the nucleation and growth processes of CuInZnS. It creates a defect regulation in CuInZnS and results in thinner 2D nanosheets of CuInZnS with a bigger specific surface area and larger pore size than those of the pristine CuInZnS. The hybrid 2D $Ti_3C_2T_x$-CuInZnS exhibits a CO production rate of 42.8 μmol g^{-1} h^{-1} in PCO_2RR.[37] With the proper synthetic routes, escalated hierarchical structures such as leaf/flower/litchi-like nanostructures can be fabricated through 2D nanostructures.[38] As aforementioned, Zhu et al. constructed the heterojunction in a heterostructure of $ZnIn_2S_4$–CdS for PCO_2RR.[31] The authors also took advantage of the hierarchical structure construction by anchoring 0D CdS quantum dots on the 3D $ZnIn_2S_4$ nanoflowers, which contributes to better charge transfer and separation during PCO_2RR. Other than the stacked 2D nanosheets/nanofibers to construct hierarchical structures, the 3D core-shell structure is also a hot topic in this field. Li et al. reported a 3D core-shell heterostructure made of c-TiO_2@a$TiO_{2-x}(OH)_y$ with HO–Ti–[O]–Ti surface frustrated Lewis pairs (SFLPs) on the shell in PCO_2RR.[39] Fig. 8a illustrates that the SFLPs dissociate dihydrogen, forming hydrides and charge-balancing protonated hydroxyl groups at unsaturated Ti sites on the surface of the catalyst to promote the PCO_2RR performance. The crystalline-amorphous heterostructure prolongs the lifetime of the electron/hole carriers (Fig. 8b). It allows a CO production rate of 5.3 mmol g^{-1} h^{-1} which is 350 times of the original c-TiO_2 catalyst.

Wei et al. developed a hollow multi-shelled structure (HoMS) of CeO_2@CeO_2/TiO_2 for CH_4 production in PCO_2RR. The high-angle annular dark field scanning TEM (HAADF-STEM) and X-ray energy dispersive spectral (EDS) mapping images in Fig. 8e and f present the multi-shelled structure of CeO_2@CeO_2/TiO_2. The quadruple inner shells are made of CeO_2, which reduces CO_2 into CO accumulated within the multi-shelled structure. The amorphous outer shell is made of TiO_2, which further converts the accumulated CO into CH_4 (Fig. 8g). The tandem CO_2–CO–CH_4 reaction of the HoMS CeO_2@CeO_2/TiO_2 affords the CO and CH_4 production rates of 97.6 μmol g^{-1} h^{-1} and 15 μmol g^{-1} h^{-1}, respectively (Fig. 8c and d). The HoMS structure can be destroyed by grinding CeO_2@CeO_2/TiO_2 into debris, causing a dramatic catalytic performance decrease (CH_4 production rate of 3.4 μmol g^{-1} h^{-1}). The control experiment highlights the significance of the hierarchical structure for the tandem reaction in PCO_2RR.[40] It reveals that the rational structure construction strategy of hybrid catalysts can further promote catalytic performance by combining different functional semiconductors to achieve a complex reaction of PCO_2RR for high-value-added products.

The production of C_{2+} is difficult for CO_2RR. Cu-based materials are the most known metal catalysts to facilitate the C–C coupling for the formation of C_{2+} products.[41] Many Cu-based photocatalysts show catalytic activities towards the production of C_{2+} products, such as In–Cu SA/PCN for CH_3CH_2OH production,[42] P/Cu SAs@CN for C_2H_6 production[43] and NiCo SA-TiO_2 for the CH_3COOH production.[44] With the assistance of the hierarchical structure engineering strategy, Cu-based photocatalysts demonstrate promising activity toward C_{2+} production in PCO_2RR. Chakraborty et al. applied the operando surface reconstruction of Wurtzite phase $CuGaS_2$ to form a 2D CuO layer-modified $CuGaS_2$, which led to a C_2H_4 production of 20.6 μmol g^{-1} h^{-1} with a selectivity of 75.1% in PCO_2RR.[45] Jia et al. grew p-type Cu_2O selectively on an Au bipyramid with the assistance of CTAB, fabricating a hetero-structure of dumbbell top which spatially separate Au and CuO

active catalysts in an hybrid photocatalyst Au/CuO. Taking advantage of both the structural engineering and the LSPR effect, dumbbell-shaped Au/CuO affords much larger C_{2+} productions under near-infrared irradiation than under visible light irradiation.[46]

4. Single-atom catalyst (SAC) strategy for PCO_2RR

Nowadays, atomically dispersed catalysts and single-atom catalysts (SACs) have gained much attention for their maximum active site utilization and superior catalytic performance.[47,48] SACs have commonly supported metal catalysts that consist of isolated monometallic moieties (single metal atoms surrounded by neighboring atoms within the support), which offer well-defined active sites in the catalysts.[49,50] Integrating the state-of-art highly active SACs with semiconductor substrates holds great promise in the catalytic performance enhancement of PCO_2RR. Anchoring the metal atoms on the substrate catalysts is currently one of the most common strategies to construct SAs such as Au, Ag, and Pt SAs on graphene.[51] Ou et al. fabricated Au SAs on red P support (Au_1/RP) with low electronegativity to absorb CO_2 for PCO_2RR.[52] RP is a single-element constituent, which provides a uniform coordination environment for Au SAs. Fig. 9a–e depicts that Au SAs are evenly distributed on the RP support. Au_1/RP affords a C_2H_6 production rate of 1.32 μmol g^{-1} h^{-1} with a selectivity of 96% (Fig. 9f). The turnover frequency (TOF) also reaches 7.39 h^{-1}, which is pretty high among many photocatalysts (Fig. 9g). The CO_2 adsorption analysis (Fig. 9h) and the in-situ diffuse reflectance infrared Fourier-transform spectroscopy (DRIFTS, Fig. 9i) confirm that Au_1/RP provides better CO_2 adsorption and activation than pure RP. It is suggested that the P atoms around the Au SAs are electron-rich and capable of serving as active sites for CO_2 activation. In the meantime, the Au SAs can decrease the C–C coupling energy barrier for C_2H_6 production in PCO_2RR (Fig. 9j).

Metal organic frameworks (MOFs) are popular precursors and templates in the CO_2RR catalyst fabrication, as well as in the SACs synthesis.[53–55] The metal node and organic ligand structure of MOFs facilitate the formation of SAs with a post-treatment of pyrolysis.[56,57] Using MOFs as the precursors is a solid strategy to fabricate SAC-combined semiconductor catalysts. Other than the MOF strategy, the facile thermal polymerization strategy is also successful in SACs fabrication. Shi et al. reported a Cu–In dual-metal SAC by the polymerization strategy for PCO_2RR.[58] As demonstrated in Fig. 10a, the metal ion salt, urea, and MIL-68 are used as precursors to fabricate the polymer. Followed by the calcination, Cu–In dual site SACs are prepared. TEM results in Fig. 10b–d show that Cu and In are evenly distributed on the CN nanosheets with isolated atom spots. The X-ray absorption spectroscopy reveals that the coordination environments of Cu and In in CuInCN are dominated by Cu–N and In–N rather than Cu–Cu and In–In, which confirms the single Cu and In atoms in the CuInCN catalyst (Fig. 10e–p). The Cu–In dual site SAC affords the superior CO yield rate of 1.2 mmol g^{-1} h^{-1} that is almost ten times of the one of the original CN catalyst under visible light irradiation while maintaining the catalytic activities after 6 runs of the tests (Fig. 10q and r).

Besides, many novel synthetic strategies were discovered over recent years. For instance, Wang et al. applied a co-dissolution strategy to dissolve $[PtV_9O_{28}]^{7-}$ into $[V_{10}O_{28}]^{6-}$ to obtain the Pt single-atom catalyst that allowed a CH_4 production rate of 247.6 μmol g^{-1} h^{-1}, much higher than that of Pt particles.[59] The numerous possibilities for the SAC synthesis of different elements hold great potential for refining the PCO_2RR catalysts for better catalytic activities.

5. Biohybrid catalysts for PCO_2RR
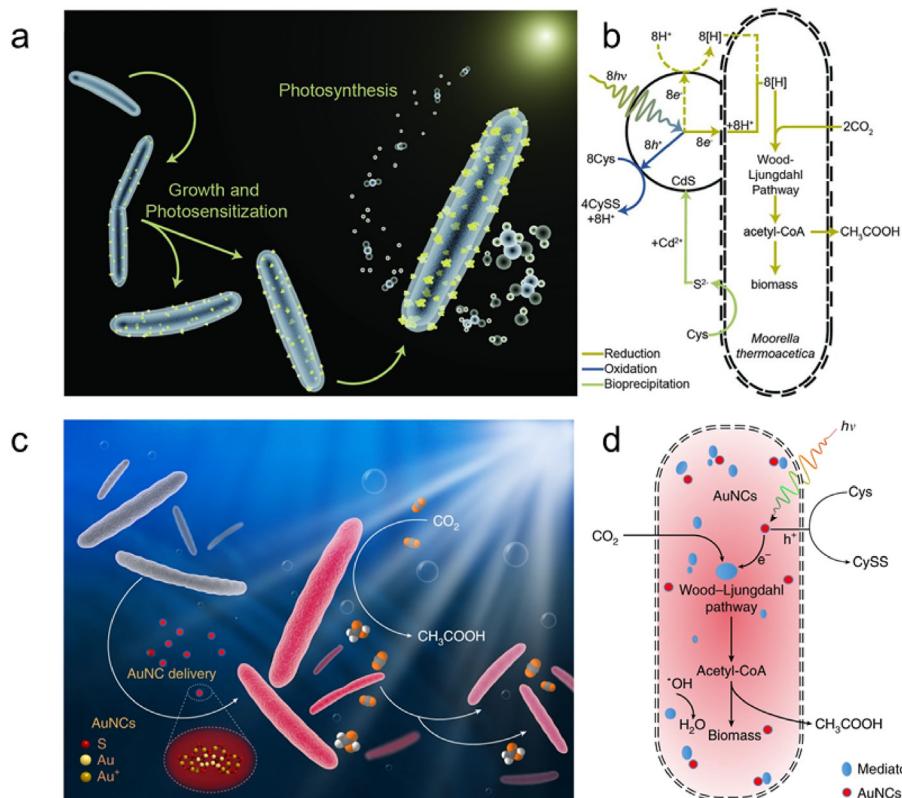
For abiotic photocatalysts, the effective transfer of the photo-generated electrons into chemical bonds for CO_2RR is challenging. Biohybrid catalysts offer alternative means for CO_2RR for the production of biofuels and biochemicals with higher product selectivity by integrating catalyst materials with biological cells.[60–66] Many successful biohybrid
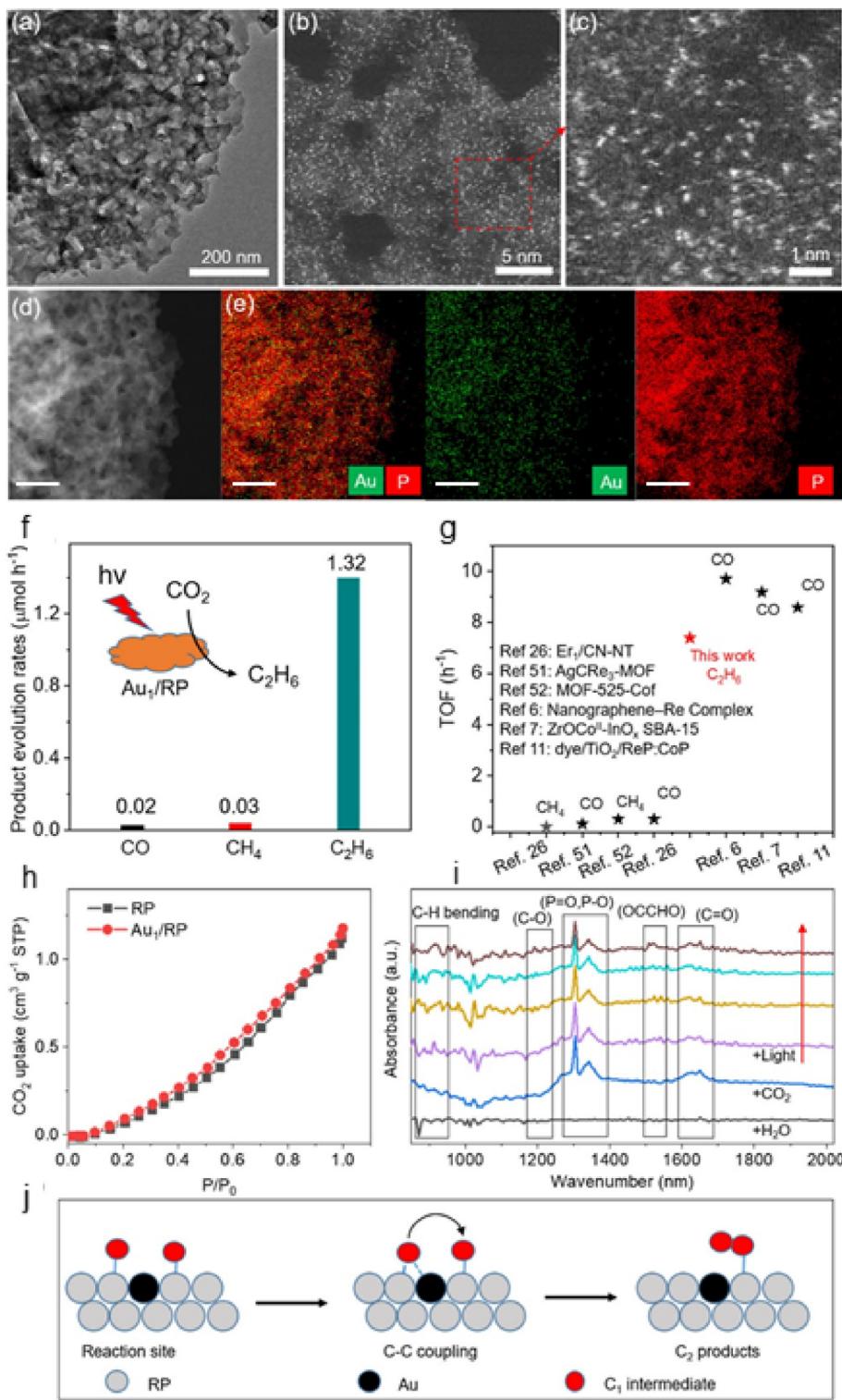
Fig. 9. (a) TEM image of Au_1/RP. (b) HAADF-STEM image and (c) enlarged image of Au_1/RP. (d) HAADF-STEM image of Au_1/RP (scale bar: 100 nm). (e) EDS mapping images of P and Au of Au_1/RP (scale bar: 100 nm). (f) PCO_2RR performance evaluation. (g) TOF values for PCO_2RR of Au_1/RP with the recently reported values in literature. (h) CO_2 adsorption of RP and Au_1/RP. (i) In-situ DRIFTS spectra of Au_1/RP for PCO_2RR. (J) Schematic of Au_1/RP for C–C coupling. Reproduced with permission from Ref. 52.

semiconductor photocatalysts have been developed for PCO_2RR. For example, moorella thermoacetica-based biohybrid photocatalysts are efficient for the production of acetic acid from CO_2, such as the self-photosensitization of moorella thermoacetica/CdS nanoparticles (Fig. 11a and b)[67] and moorella thermoacetica/Au nanoclusters (Fig. 11c and d).[68] Moreover, light-harvesting artificial cells containing cyanobacteria afford to fix CO_2 into glucose.[69]

Other than bacteria, protein can also be used in biohybrid semiconductor systems for PCO_2RR. Saif et al. designed a –NH_2 group functionalized 1D protein-encapsulated CeO_2 nanorods (PCNRs) for CO and CH_4 productions in PCO_2RR.[70] As depicted in Fig. 12a, the bovine serum albumin (BSA) is applied as an efficient biotemplate to synthesize PCNRs. With TEOA as the electron donor to consume the holes and the assistance of RhB, PCNRs demonstrate excellent activity toward H_2 production (Fig. 12b). When carried out in a CO_2 gas environment, PCNRs show catalytic activities towards CH_4 and CO productions under light irradiation of 400 nm $< \lambda <$ 780 nm (Fig. 12c) with great suppression of H_2 production. Fig. 12d and e reveal that PCNRs exhibit CO
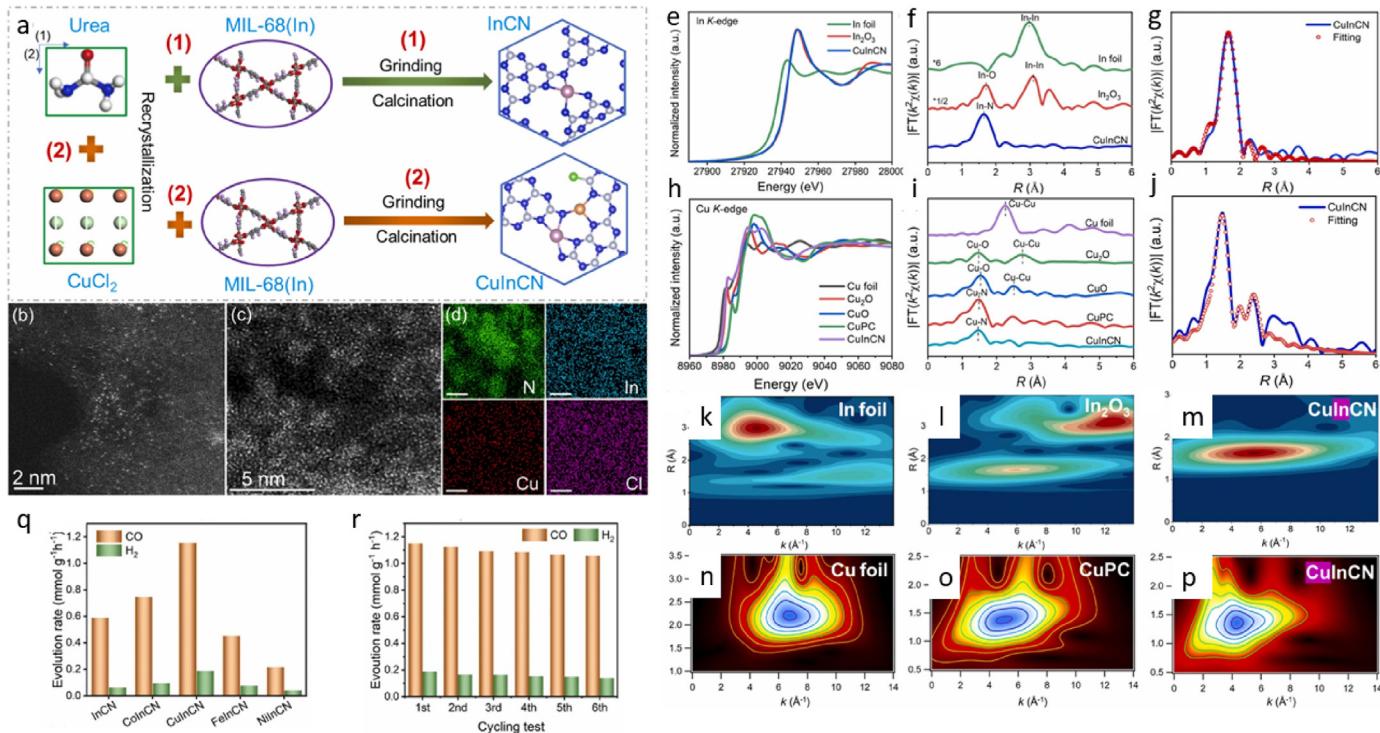
Fig. 10. (a) Schematic of the synthetic process for CuInCN and InCN (green: Cl atom, orange: Cu atom, pale purple: In atom, red: O atom, blue: N atom, light grey: C atom, white: H atom). HAADF-STEM images of (b) InCN and (c) CuInCN. (d) EDS mapping images of CuInCN (scale bar: 2 μm). (e) In K-edge XANES of CuInCN. (f) EXAFS spectra. (g) EXAFS fitting curves. (h) Cu K-edge XANES of CuInCN. (i) XAFS spectra. (j) EXAFS fitting curves. In K-edge Wavelet transforms contour plots of (k) In foil, (l) In_2O_3 and (m) CuInCN. Cu K-edge Wavelet transforms contour plots of (n) Cu foil, (o) CuPC and (p) CuInCN. (q) PCO_2RR productions on CuInCN with different Cu loadings. (r) Repeat reaction test with the reaction time of 3 h. Reproduced with permission from Ref. 58.

Fig. 11. (a) Illustration of the moorella thermoacetica–CdS bio-hybrid PCO_2RR system, yellow dots: CdS nanoparticles. CO_2 (center right) is converted to acetic acid (right). (b) Schematic of the moorella thermoacetica–CdS bio-hybrid PCO_2RR system. [H] generates outside the cell (marked in dashed line) or generated by the direct electron transport to the cell (marked in solid line). Reproduced with permission from Ref. 67. (c) Illustration of the moorella thermoacetica/AuNCs bio-hybrid PCO_2RR system. $Au_{22}(SG)_{18}$ nanoclusters are delivered into bare moorella thermoacetica (grey) during the catalyst synthesis to form moorella thermoacetica/AuNCs with red emission. Insert: the simulated chemical structure of $Au_{22}(SG)_{18}$ nanoclusters. (Au atoms in the core: light yellow spheres; Au atoms in the staple motifs: dark yellow; S atoms in the shell: red; Oxygen atoms: orange; Carbon atoms: grey; hydrogen atoms: white.) (d) Schematic of the bacterium. The photo-generated electrons in AuNCs under irradiation are utilized by the enzymatic mediators inside the cytoplasm, which pass on to the Wood–Ljungdahl pathway. Reproduced with permission from Ref. 68.

Fig. 12. (a) Schematic of the synthetic procedure of the catalyst. (b) H_2 generation reaction mechanism on the PCNRs. TEOA serves as the electron donor to consume the photo-generated hole. (c) PCO_2RR mechanism. (d) CO, CH_4, and H_2 yields during PCO_2RR on PCNRs. (e) CO, CH_4, and H_2 production rates on PCNRs and B–CeO_2 NRs. Reproduced with permission from Ref. 70.

and CH_4 production rates of 5.0 and 3.3 μmol h^{-1} g^{-1}, which are 50 and 83 times higher than those of non-biohybrid CeO_2, respectively. The authors believe that the protein hybrid PCNRs significantly enhance the material stability and facilitate the transfer of photo-generated holes to promote the separation process of photo-generated carriers.

Researchers should still pay attention to some key points, concerning the future design of biohybrid photocatalysts. First, semiconductor materials that are compatible with bio cells need to be rationally constructed to protect microbial cells from deactivation while sufficiently harvesting visible light to provide enough electrons for CO_2RR. Second, the interface of the biotic–abiotic should be tailored for quick charge transfer, accelerating the separation rate of electron/hole pairs for better catalytic performance. Finally, the integrated bio-material should be able to efficiently utilize photo-generated electrons to produce fuel chemicals from PCO_2RR.[60]

6. Characterization techniques in PCO_2RR

After the design of highly efficient catalysts, many characterization techniques are required to understand the properties and uniqueness of the photocatalyst material for excellent catalytic efficiency. X-ray photoelectron spectroscopy (XPS), X-ray powder diffraction (XRD), UV-Vis spectroscopy, and X-ray absorption spectroscopy (XAS) are common techniques for exploring the element valence, crystallization, bandgap value, and coordination environment information of the materials. Scanning electron microscopes (SEM), transmission electron microscopy (TEM), and energy dispersive spectroscopy (EDS) can directly provide visual images of morphologies and element distributions of catalyst materials. The combination

of different characterization techniques is important to confirm one's assumption. For example, the analysis of XAS and XPS helps to confirm the N/O ratio in N–Ti–O/V[O] for the production of C_{2+} products on TiO_2 catalysts.[82] For revealing the reaction mechanism of CO_2RR, the density functional theory (DFT) simulations emerge as one of the most useful tools to demystify the structure-activity relationship and catalytic mechanism for complex catalytic systems such as hybrid catalysts.[83–86] In the meantime, in-situ characterizations, such as in-situ XRD, in-situ XAS, and in-situ Raman spectroscopy, are powerful experimental approaches to trace the evolution of the catalyst structures and reaction intermediates during the catalytic reaction of CO_2RR.[87–90] Apart from Raman spectroscopy, in-situ Fourier transform infrared absorption spectroscopy (FTIR) can also provide evidence of reaction intermediates, uncovering the reaction pathway of CO_2RR.[91,92] Wu et al. prepared an oxygen vacancy (V_o)-rich MoO_{2-x} for PCO_2RR.[93] The V_o-rich MoO_{2-x} exhibits a CH_4 production rate of 5.8 and 12.2 μmol g^{-1} h^{-1} under NIR and full light irradiation in PCO_2RR, which is around 10- and 7-fold to those of the V_o-poor MoO_{2-x}, respectively (Fig. 13a). Besides, the V_o-rich MoO_{2-x} performs PCO_2RR directly under an air atmosphere with a CO production rate of 6.5 μmol g^{-1} h^{-1} under NIR irradiation (Fig. 13b). V_o-rich MoO_{2-x} also demonstrates good stability in PCO_2RR activity under NIR irradiation in concentrated CO_2 after 4 runs (Fig. 13c). In-situ FTIR is applied to reveal the reaction mechanism of PCO_2RR over the MoO_{2-x} catalysts. Fig. 13d shows that carbonate species and *CO_2^- appear in the dark, suggesting the absorption and activation of CO_2 on the V_o-rich MoO_{2-x} surface. Additional peaks of *COOH (1593 cm^{-1}), *CH_3O (1170 and 1100 cm^{-1}), and *CHO (1082 cm^{-1}) appear, and are gradually strengthened with the increase of illumination time under NIR (Fig. 13e). These intermediates are essential to the
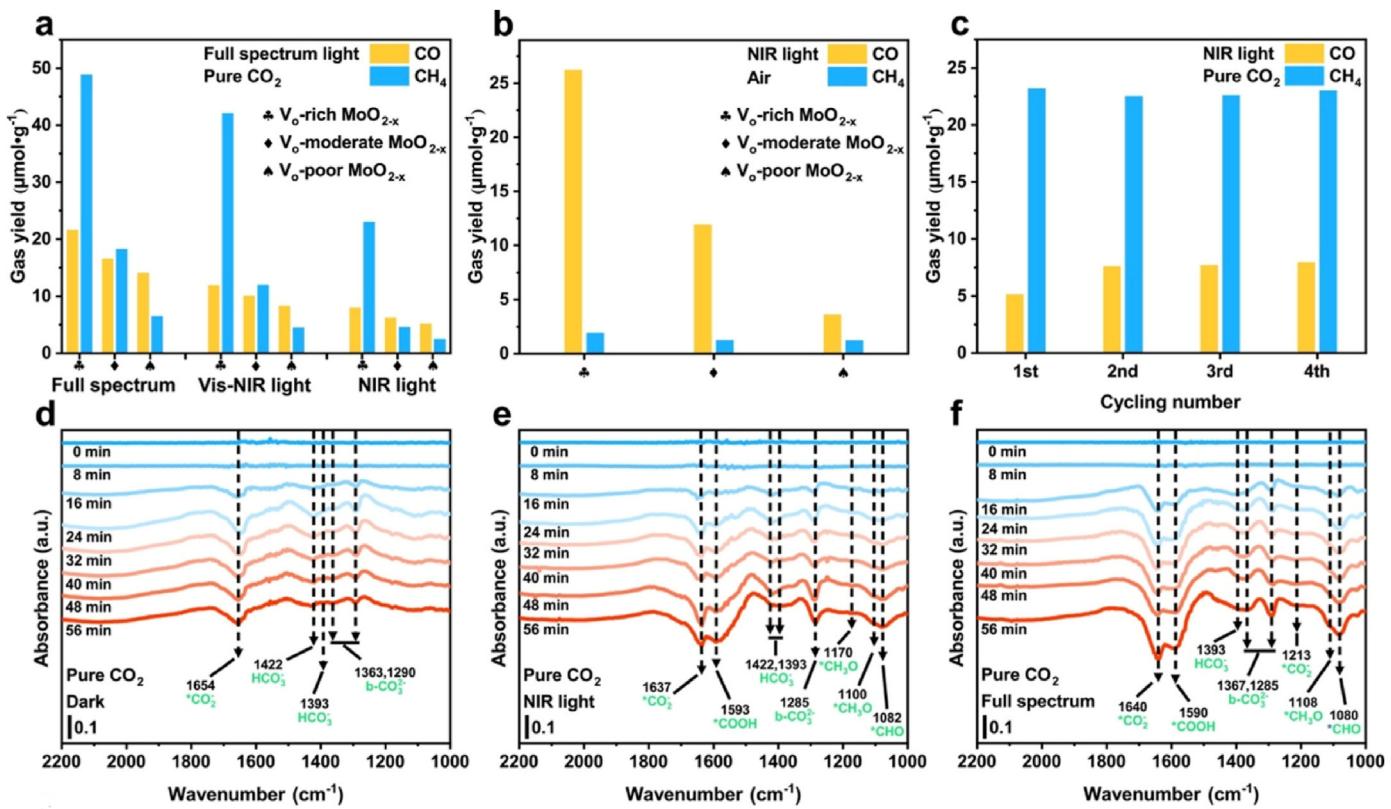
Fig. 13. PCO$_2$RR performance on MoO$_{2-x}$ under (a) whole light illumination in pure CO$_2$, (b) NIR illumination in air, and (c) repeat tests of PCO$_2$RR under NIR illumination in pure CO$_2$. In-situ FTIR experiments on V$_o$-rich MoO$_{2-x}$ (d) under the dark, (e) under NIR illumination, and (f) under whole light illumination in pure CO$_2$. Reproduced with permission from Ref. 93.

production of CH$_4$ in CO$_2$RR. When illuminated under full spectrum light, the IR peak intensities of the intermediates further increased (Fig. 13f). It reveals the efficient light response of V$_o$-rich MoO$_{2-x}$ and the possible reaction pathway (CO$_2$→*CO$_2$→*COOH→*CO→COor*CHO→*CH$_2$O →*CH$_3$O→CH$_4$) for PCO$_2$RR.

With the advance of characterization techniques, powerful characteristic techniques are exploited for revealing the compositional effects in hybrid catalysts. Chen et al. recently applied spatiotemporally-resolved surface photovoltage measurements (SPVM) on the facet and defect-engineered Cu$_2$O catalysts (Fig. 14a) to map the holistic charge transfer processes at the single-particle level on the femtosecond timescale.[94] Fig. 14b depicts that the {001} facet has more accumulated photo-generated electrons than the {111} facet of the Cu$_2$O octahedron, owing to the high Cu vacancies (V$_{Cu}$) on the {001} facet. Fig. 14c demonstrates that the anisotropic charge transfer is optimized with a truncated octahedral configuration, suggesting the contribution of the inter-facet built-in electric field to the anisotropic charge transfer. SPVM in Fig. 14d further illustrates that the moderate hydrogen-compensated V$_{Cu}$ (H–V$_{Cu}$) results in an efficient spatial separation of the photo-generated carriers on {111} and {001} facets. On the contrary, the extreme incorporation of H–V$_{Cu}$ leads to the quench of the photo-generated electron/hole pairs (Fig. 14e). The photoemission electron images in Fig. 14f visualize the dynamics of anisotropic electron transfer for single Cu$_2$O particle, indicating that the ultrafast inter-facet electron transfer contributes significantly to the anisotropic electron distribution. Au selectively deposited on the {001} facet of Cu$_2$O can also be successfully probed by SPVM (Fig. 14g–i). It is confirmed that the H$_2$ evolution performance is associated with the anisotropic charge transfer of Cu$_2$O (Fig. 14j). This powerful SPVM technique brings meaningful insights into the photo-carrier transfer dynamics, which can be transplanted to PCO$_2$RR. With more advanced characterization techniques developed and applied to the PCO$_2$RR catalysts, the rational design of the

next-generation photocatalyst for excellent catalytic performance can be precisely and systematically guided.

7. Perspectives

To sum up, semiconductor photocatalysts often suffer from unsatisfying catalytic performance (e.g. with production rate at the level of μmol g^{-1} h^{-1}) in PCO$_2$RR, owing to the poor light harvesting ability, the low separation rate of the photo-induced carriers, and stability issues. Designing novel semiconductor materials with highly efficient catalytic performance for PCO$_2$RR that address these issues is a priority. The hybridization of semiconductor catalysts through different approaches such as surface modification and band engineering strategies can integrate the advantages of the different semiconductor catalysts and co-catalysts to prohibit the recombination of the photo-generated electron/hole pairs and promote the light response of the semiconductor catalysts for PCO$_2$RR. The hierarchical structure construction of semiconductor catalysts also contributes to the separation of the photo-generated electron/ hole pairs and sometimes can even achieve a spatially coordinated tandem reaction to produce C$_{2+}$ products from PCO$_2$RR. Active sites are essential to catalysis. Anchoring highly catalytically effective SACs on semiconductor catalysts holds great promise for the augmentation of catalytic activities in PCO$_2$RR. To improve product selectivity, integrating biological materials that are highly selective in photosynthesis with semiconductor catalysts has been proven to be an effective solution. Moreover, by using advanced characterization techniques for in-situ probing, the underlying mechanism of the reaction pathway and catalyst structure evolution can be demystified for next-generation PCO$_2$RR catalyst design. Other than the proposed solutions discussed above, current research on PCO$_2$RR still needs to focus on the following perspectives:
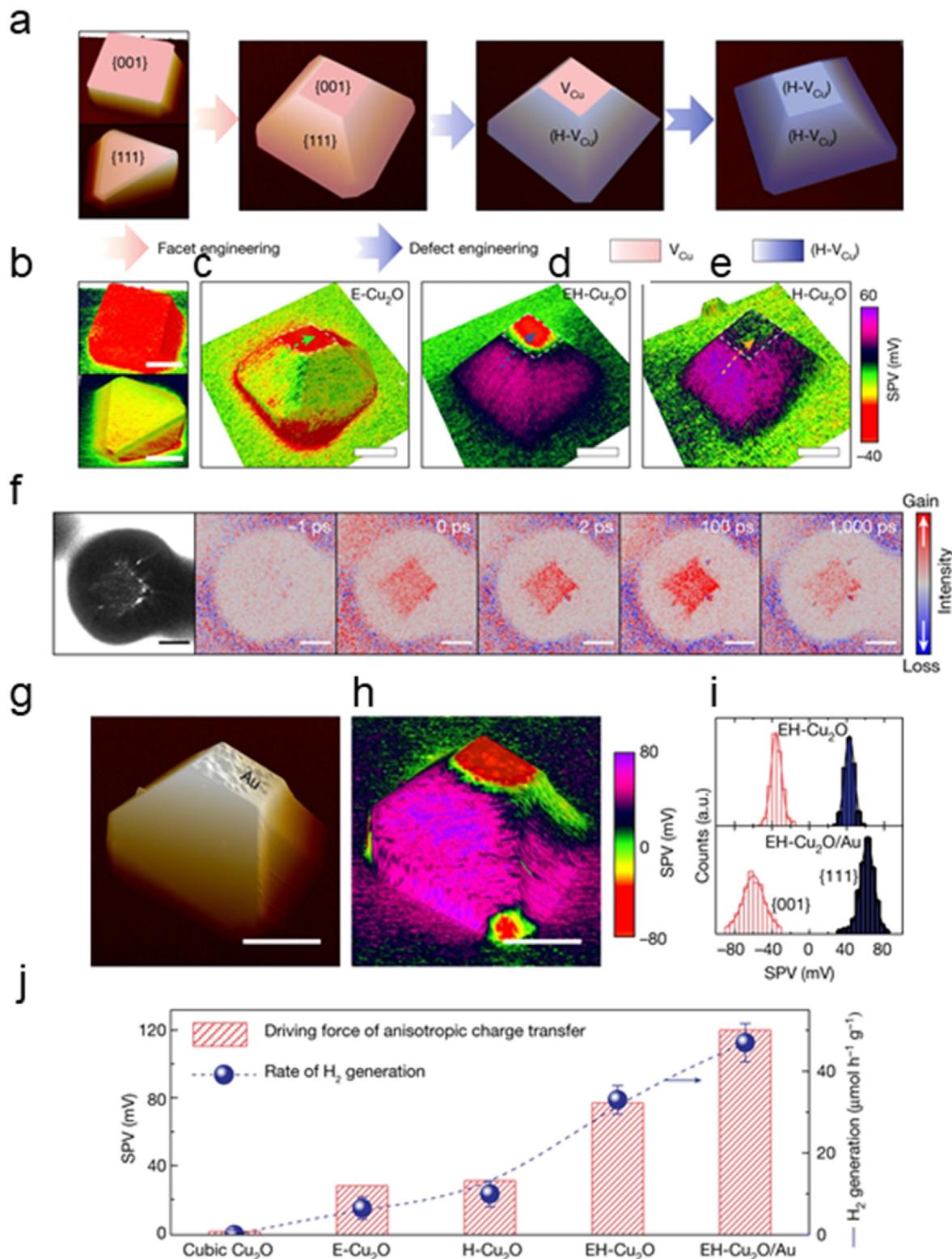
Fig. 14. (a) Schematic of the anisotropic facets and defects engineering on Cu₂O particles. (b) SPVM images of octahedral (bottom) and cubic (top) Cu₂O particles. SPVM images of truncated octahedral Cu₂O particles of (c) without incorporation of (H–VCu) defects, (d) with moderate incorporation of (H–VCu) defects, and (e) with extreme incorporation of (H–VCu) defects. Time-resolved photoemission electron microscopy of E-Cu₂: (f) PEEM image and a series of TR-PEEM images of EH-Cu₂O O at different pump-probe delay times, as labeled. Scale bars: 2 μm. (g) AMF image and (h) corresponding SPVM image of EH-Cu₂O O/Au. (i) Comparison of the statistical SPV signals on the {001} and {111} facets of EH-Cu₂O with Au particles selectively deposited on the {001} facet (marked as EH-Cu₂O/Au. (j) Driving forces of the anisotropic charge transfer and the PCO₂RR performance. Reproduced with permission from Ref. 94.

(1) The duration of the catalytic performance is always a big issue in PCO$_2$RR. Most photocatalysts present a catalytic activity duration of dozens of hours, which is excessively low for industrial requirements (more than thousands of hours).[95,96] The fabrication of highly active semiconductor materials for CO$_2$RR without accumulating residues of poisoning intermediates is forever a priority. Besides, the addition of the protective layer on the surface of photocatalysts to mitigate the decay of the catalyst structure during PCO$_2$RR could be a possible solution to enhance the catalyst stability.[7]

(2) In addition, the combination of photocatalysis with other catalytic methods such as electrochemical catalysis and thermal catalysis (e.g. photo-electrocatalysis) holds great potential to improve both the catalytic activities and product selectivity in CO$_2$RR.[97,98] CO$_2$ capture and storage (CCS) takes a vital part in the mitigation of over-emitted CO$_2$, because it is energy-consuming.[99] Sorbent porous materials such as metal oxides,[100–102] zeolites and amine-functionalized silicas,[103] covalent organic frameworks (COFs),[104–106] MOFs,[107–109] and porous carbons[110] are effective toward CO$_2$ captures. Many of these sorbent materials also demonstrate photocatalytic activity towards CO$_2$RR. Hence, coupling CO$_2$-capture with PCO$_2$RR can be a practical means in the further market for better efficiency.[111–115]

(3) To finally achieve a practical application, a rational catalysis setup needs to be designed for high catalytic efficiency and scale-up production. Many promising CO$_2$RR systems have been developed for electrolysis, such as gas phase flow cells, solid oxide electrolysis cells (SOECs), etc.[116–118] For the photocatalysis-related setup upgrade, there are also some interesting discoveries, e.g., the back-illuminated photo-electrochemical flow cell for the increased solar-to-fuel conversion efficiency,[119] and the aerobic environment for the improved PCO$_2$RR in a less restricted reaction condition.[120]

Declaration of competing interest

There is no conflict of interest to declare.

Acknowledgments

References

1. Su JJ, Liu Y, Song Y, et al. Recent development of nanomaterials for carbon dioxide electroreduction. *Smartmat*. 2022;3(1):35–53.

2. Wang Y, Chen E, Tang J. Insight on reaction pathways of photocatalytic CO$_2$ conversion. *ACS Catal*. 2022;12(12):7300–7316.

3. Chen Z, Zhang G, Du L, et al. Nanostructured cobalt-based electrocatalysts for CO$_2$ reduction: recent progress, challenges, and perspectives. *Small*. 2020;16(52), e2004158.

4. Wang R, Wang X, Xiong Y, et al. Modulation of trivalent/tetravalent metallic elements in Ni-based layered double hydroxides for photocatalytic CO$_2$ reduction. *ACS Appl Mater Interfaces*. 2022;14(31):35654–35662.

5. Maeda K. Metal-complex/semiconductor hybrid photocatalysts and photoelectrodes for CO$_2$ reduction driven by visible light. *Adv. Mater*. 2019;31(25), e1808205.

6. Zhang W, Mohamed AR, Ong WJ. Z-Scheme photocatalytic systems for carbon dioxide reduction: where are we now? *Angew Chem, Int Ed Engl*. 2020;59(51): 22894–22915.

7. Chen ZS, Zhang GX, Prakash J, et al. Rational design of novel catalysts with atomic layer deposition for the reduction of carbon dioxide. *Adv Energy Mater*. 2019;9(37), 1900889.

8. An L, De La Torre P, Smith PT, et al. Synergistic porosity and charge effects in a supramolecular porphyrin cage promote efficient photocatalytic CO$_2$ reduction. *Angew Chem, Int Ed Engl*. 2023;62(5), e202209396.

9. Yu Y, Dong X, Chen P, et al. Synergistic effect of Cu single atoms and Au-Cu alloy nanoparticles on TiO$_2$ for efficient CO$_2$ photoreduction. *ACS Nano*. 2021;15(9): 14453–14464.

10. Yoshida H, Zhang L, Sato M, et al. Calcium titanate photocatalyst prepared by a flux method for reduction of carbon dioxide with water. *Catal Today*. 2015;251: 132–139.

11. Dong Y, Duchesne P, Mohan A, et al. Shining light on CO$_2$: from materials discovery to photocatalyst, photoreactor and process engineering. *Chem Soc Rev*. 2020; 49(16):5648–5663.

12. Wang JW, Ma F, Jin T, et al. Homoleptic Al(III) photosensitizers for durable CO$_2$ photoreduction. *J Am Chem Soc*. 2023;145(1):676–688.

13. Das R, Paul R, Parui A, et al. Engineering the charge density on an In$_{2.77}$S$_4$/porous organic polymer hybrid photocatalyst for CO$_2$-to-ethylene conversion reaction. *J Am Chem Soc*. 2023;145(1):422–435.

14. Liang YJ, Wu X, Liu XY, et al. Recovering solar fuels from photocatalytic CO$_2$ reduction over W$_6^+$-incorporated crystalline g-C$_3$N$_4$ nanorods by synergetic modulation of active centers. *Appl Catal B Environ*. 2022;304, 120978.

15. Liang MF, Borjigin T, Zhang YH, et al. Controlled assemble of hollow heterostructured g-C$_3$N$_4$@CeO$_2$ with rich oxygen vacancies for enhanced photocatalytic CO$_2$ reduction. *Appl Catal B Environ*. 2019;243:566–575.

16. Li B, Si Y, Zhou BX, et al. Doping-induced hydrogen-bond engineering in polymeric carbon nitride to significantly boost the photocatalytic H$_2$ evolution performance. *ACS Appl Mater Interfaces*. 2019;11(19):17341–17349.

17. Shi X, Dong XA, He Y, et al. Photoswitchable chlorine vacancies in ultrathin Bi$_4$O$_5$Cl$_2$ for selective CO$_2$ photoreduction. *ACS Catal*. 2022;12(7):3965–3973.

18. Wang Q, Miao Z, Zhang Y, et al. Photocatalytic reduction of CO$_2$ with H$_2$O mediated by Ce-tailored bismuth oxybromide surface frustrated Lewis pairs. *ACS Catal*. 2022;12(7):4016–4025.

19. Wang N, Cheong S, Yoon DE, et al. Efficient, selective CO$_2$ photoreduction enabled by facet-resolved redox-active sites on colloidal CdS nanosheets. *J Am Chem Soc*. 2022;144(37):16974–16983.

20. Tan L, Xu SM, Wang Z, et al. Highly selective photoreduction of CO$_2$ with suppressing H$_2$ evolution over monolayer layered double hydroxide under irradiation above 600 nm. *Angew Chem, Int Ed Engl*. 2019;58(34):11860–11867.

21. Wang X, Wang ZL, Bai Y, et al. Tuning the selectivity of photoreduction of CO$_2$ to syngas over Pd/layered double hydroxide nanosheets under visible light up to 600 nm. *J Energy Chem*. 2020;46:1–7.

22. Ma Y, Yi X, Wang S, et al. Selective photocatalytic CO$_2$ reduction in aerobic environment by microporous Pd-porphyrin-based polymers coated hollow TiO$_2$. *Nat Commun*. 2022;13(1):1400.

23. Huang H, Shi R, Li Z, et al. Triphase photocatalytic CO$_2$ reduction over silver-decorated titanium oxide at a gas-water boundary. *Angew Chem, Int Ed Engl*. 2022; 61(17), e202200802.

24. Yue X, Cheng L, Li F, et al. Highly strained Bi-MOF on bismuth oxyhalide support with tailored intermediate adsorption/desorption capability for robust CO$_2$ photoreduction. *Angew Chem, Int Ed Engl*. 2022;61(40), e202208414.

25. Jiang Y, Yu Y, Zhang X, et al. N-heterocyclic carbene-stabilized ultrasmall gold nanoclusters in a metal-organic framework for photocatalytic CO$_2$ reduction. *Angew Chem, Int Ed Engl*. 2021;60(32):17388–17393.

26. Shangguan W, Liu Q, Wang Y, et al. Molecular-level insight into photocatalytic CO$_2$ reduction with H$_2$O over Au nanoparticles by interband transitions. *Nat Commun*. 2022;13(1):3894.

27. Zhu K, Zhu Q, Jiang M, et al. Modulating Ti t$_{2g}$ orbital occupancy in a Cu/TiO$_2$ composite for selective photocatalytic CO$_2$ reduction to CO. *Angew Chem, Int Ed Engl*. 2022;61(34), e202207600.

28. Hu C, Chen X, Low J, et al. Near-infrared-featured broadband CO$_2$ reduction with water to hydrocarbons by surface plasmon. *Nat Commun*. 2023;14(1):221.

29. He X, Kai T, Ding P. Heterojunction photocatalysts for degradation of the tetracycline antibiotic: a review,. *Environ Chem Lett*. 2021;19(6):4563–4601.

30. Chen Q, Lan X, Ma Y, et al. Boosting CsPbBr$_3$-driven superior and long-term photocatalytic CO$_2$ reduction under pure water medium: synergy effects of multifunctional melamine foam and graphitic carbon nitride (g-C$_3$N$_4$). *Solar RRL*. 2021;5(7), 2100186.

31. Zhu ZZ, Li XX, Qu YT, et al. A hierarchical heterostructure of CdS QDs confined on 3D ZnIn$_2$S$_4$ with boosted charge transfer for photocatalytic CO$_2$ reduction,. *Nano Res*. 2021;14(1):81–90.

32. Wang XT, Wang ZZ, Li Y, et al. Efficient photocatalytic CO$_2$ conversion over 2D/2D Ni-doped CsPbBr$_3$/Bi$_3$O$_4$Br Z-scheme heterojunction: critical role of Ni doping, boosted charge separation and mechanism study. *Appl Catal B Environ*. 2022;319, 121895.

33. Long L, Lv G, Han Q, et al. Achieving direct Z-scheme charge transfer through constructing 2D/2D α-Fe$_2$O$_3$/CdS heterostructure for efficient photocatalytic CO$_2$ conversion. *J Phys Chem C*. 2021;125(42):23142–23152.

34. Wang Q, Warnan J, Rodriguez-Jimenez S, et al. Molecularly engineered photocatalyst sheet for scalable solar formate production from carbon dioxide and water. *Nat Energy*. 2020;5(9):703–710.

35. Bai S, Ning C, Wang H, et al. VO$_4$-modified layered double hydroxides nanosheets for highly selective photocatalytic CO$_2$ reduction to C$_1$ products. *Small*. 2022; 18(40), e2203787.

36. Liang J, Yu H, Shi J, et al. Dislocated bilayer MOF enables high-selectivity photocatalytic reduction of CO$_2$ to CO. *Adv Mater*. 2023;35(10), e2209814.

37. Wang LJ, Zhang Z, Guan RQ, et al. Synergistic CO_2 reduction and tetracycline degradation by CuInZnS-$Ti_3C_2T_x$ in one photoredox cycle. *Nano Res*. 2022;15(9):8010–8018.
38. Hiragond C, Ali S, Sorcar S, et al. Hierarchical nanostructured photocatalysts for CO_2 photoreduction. *Catalysts*. 2019;9(4):370.
39. Li Z, Mao C, Pei Q, et al. Engineered disorder in CO_2 photocatalysis. *Nat Commun*. 2022;13(1):7205.
40. Wei Y, You F, Zhao D, et al. Heterogeneous hollow multi-shelled structures with amorphous-crystalline outer-shells for sequential photoreduction of CO_2. *Angew Chem, Int Ed Engl*. 2022;61(49), e202212049.
41. Wang XD, Hu Q, Li GD, et al. Recent advances and perspectives of electrochemical CO_2 reduction toward C_{2+} products on Cu-based catalysts. *Electrochem Energy Rev*. 2022;5(Suppl 2):28.
42. Shi H, Wang H, Zhou Y, et al. Atomically dispersed indium-copper dual-metal active sites promoting C-C coupling for CO_2 photoreduction to ethanol. *Angew Chem, Int Ed Engl*. 2022;61(40), e202208904.
43. Wang G, Chen Z, Wang T, et al. P and Cu dual sites on graphitic carbon nitride for photocatalytic CO_2 reduction to hydrocarbon fuels with high C_2H_6 evolution. *Angew Chem, Int Ed Engl*. 2022;61(40), e202210789.
44. Jia G, Sun M, Wang Y, et al. Asymmetric coupled dual-atom sites for selective photoreduction of carbon dioxide to acetic acid. *Adv Funct Mater*. 2022;32(41), 2206817.
45. Chakraborty S, Das R, Riyaz M, et al. Wurtzite $CuGaS_2$ with an in-situ-formed CuO layer photocatalyzes CO_2 conversion to ethylene with high selectivity. *Angew Chem, Int Ed Engl*. 2023;62(9), e202216613.
46. Jia H, Li F, Chow TH, et al. Construction of spatially separated gold nanocrystal/cuprous oxide architecture for plasmon-driven CO_2 reduction. *Nano Lett*. 2022;22(17):7268–7274.
47. Hulva J, Meier M, Bliem R, et al. Unraveling CO adsorption on model single-atom catalysts. *Science*. 2021;371(6527):375–379.
48. Vijay S, Gauthier JA, Heenen HH, et al. Dipole-field interactions determine the CO_2 reduction activity of 2D Fe-N-C single-atom catalysts. *ACS Catal*. 2020;10(14):7826–7835.
49. Jeong H, Kwon O, Kim BS, et al. Highly durable metal ensemble catalysts with full dispersion for automotive applications beyond single-atom catalysts. *Nat Catal*. 2020;3(4):368–375.
50. Chen ZS, Zhang GX, Chen HR, et al. Multi-metallic catalysts for the electroreduction of carbon dioxide: recent advances and perspectives. *Renew Sustain Energy Rev*. 2022;155, 111922.
51. Guo S, Song C, Liu F, et al. Bionic optical leaf for photoreduction of CO_2 from noble metal atom mediated graphene nanobubble arrays. *ACS Nano*. 2022;16(2):1909–1918.
52. Ou H, Li G, Ren W, et al. Atomically dispersed Au-assisted C-C coupling on red phosphorus for CO_2 photoreduction to C_2H_6. *J Am Chem Soc*. 2022;144(48):22075–22082.
53. Wang X, Zou Y, Zhang Y, et al. Tin-based metal organic framework catalysts for high-efficiency electrocatalytic CO_2 conversion into formate. *J Colloid Interface Sci*. 2022;626:836–847.
54. Guan Y, Zhang X, Zhang Y, et al. Achieving high selectivity towards electro-conversion of CO_2 using In-doped Bi derived from metal-organic frameworks. *J Colloid Interface Sci*. 2022;612:235–245.
55. Wang XY, Fan MY, Guan YY, et al. MOF-based electrocatalysts for high-efficiency CO_2 conversion: structure, performance, and perspectives. *J Mater Chem*. 2021;9(40):22710–22728.
56. Cho JH, Lee C, Hong SH, et al. Transition metal ion doping on ZIF-8 enhances the electrochemical CO_2 reduction reaction. *Adv Mater*. 2022, e2208224.
57. Chen Z, Zhang G, Wen Y, et al. Atomically dispersed Fe-Co bimetallic catalysts for the promoted electroreduction of carbon dioxide. *Nano-Micro Lett*. 2021;14(1):25.
58. Shi HN, Li JH, Wang HZ, et al. Chlorine tailored p-d blocks dual-metal atomic catalyst for efficient photocatalytic CO_2 reduction. *Appl Catal B Environ*. 2023;322, 122139.
59. Wang YJ, Zhuang GL, Zhang JW, et al. Co-dissolved isostructural polyoxovanadates to construct single-atom-site catalysts for efficient CO_2 photoreduction. *Angew Chem, Int Ed Engl*. 2023;62(6), e202216592.
60. Zhang J, Liu LM, Chen XL. Pushing hybrids to the limits. *Nat Catal*. 2022;5(11):975–976.
61. Zhou X, Zeng Y, Lv F, et al. Organic semiconductor-organism interfaces for augmenting natural and artificial photosynthesis. *Acc Chem Res*. 2022;55(2):156–170.
62. Zhou Y, Guo X, Li X, et al. Effect of different soaking time on catalytic performance of CuO/Cu@BC electrode for CO_2 reduction. *Chin J Process Eng*. 2020;20(8):989–996.
63. Kim J, Cestellos-Blanco S, Shen YX, et al. Enhancing biohybrid CO_2 to multicarbon reduction via adapted whole-cell catalysts. *Nano Lett*. 2022;22(13):5503–5509.
64. Cobb SJ, Badiani VM, Dharani AM, et al. Fast CO_2 hydration kinetics impair heterogeneous but improve enzymatic CO_2 reduction catalysis. *Nat Chem*. 2022;14(4):417–424.
65. Contaldo U, Curtil M, Perard J, et al. A Pyrene-triazacyclononane anchor affords high operational stability for CO_2RR by a CNT-supported histidine-tagged CODH. *Angew Chem, Int Ed Engl*. 2022;61(21), e202117212.
66. Wang Q, Kalathil S, Pornrungroj C, et al. Bacteria-photocatalyst sheet for sustainable carbon dioxide utilization. *Nat Catal*. 2022;5(7):633–641.
67. Sakimoto KK, Wong AB, Yang P. Self-photosensitization of nonphotosynthetic bacteria for solar-to-chemical production. *Science*. 2016;351(6268):74–77.
68. Zhang H, Liu H, Tian Z, et al. Bacteria photosensitized by intracellular gold nanoclusters for solar fuel production. *Nat Nanotechnol*. 2018;13(10):900–905.
69. Yang B, Li S, Mu W, et al. Light-harvesting artificial cells containing cyanobacteria for CO_2 fixation and further metabolism mimicking. *Small*. 2022, e2201305.
70. Saif B, Gu Q, Yang P. The synthesis of protein-encapsulated ceria nanorods for visible-light driven hydrogen production and carbon dioxide reduction,. *Small*. 2021;17(45), e2103422.
71. Wang Y, Fan G, Wang S, et al. Implanting CoO_x clusters on ordered macroporous ZnO nanoreactors for efficient CO_2 photoreduction. *Adv Mater*. 2022;34(42), e2204865.
72. Zhang G, Wang F, Tubul T, et al. Complexed semiconductor cores activate hexaniobate ligands as nucleophilic sites for solar-light reduction of CO_2 by water. *Angew Chem, Int Ed Engl*. 2022;61(49), e202213162.
73. Deng Y, Wan CA, Li C, et al. Synergy effect between facet and zero-valent copper for selectivity photocatalytic methane formation from CO_2. *ACS Catal*. 2022;12(8):4526–4533.
74. Wang L, Wang R, Qiu T, et al. Bismuth vacancy-induced efficient CO_2 photoreduction in BiOCl directly from natural air: a progressive step toward photosynthesis in nature,. *Nano Lett*. 2021;21(24):10260–10266.
75. Zhao L, Bian J, Zhang X, et al. Construction of ultrathin s-scheme heterojunctions of single Ni atom immobilized Ti-MOF and $BiVO_4$ for CO_2 photoconversion of nearly 100% to CO by pure water. *Adv. Mater*. 2022;34(41), 2205303.
76. Ding J, Tang Q, Fu Y, et al. Core-shell covalently linked graphitic carbon nitride-melamine-resorcinol-formaldehyde microsphere polymers for efficient photocatalytic CO_2 reduction to methanol. *J Am Chem Soc*. 2022;144(22):9576–9585.
77. Hu J, Yang T, Yang X, et al. Highly selective and efficient solar-light-driven CO_2 conversion with an ambient-stable 2D/2D $Co_2P@BP/g-C_3N_4$ heterojunction. *Small*. 2022;18(7), e2105376.
78. Sun X, Sun L, Li G, et al. Phosphorus tailors the d-band center of copper atomic sites for efficient CO_2 photoreduction under visible-light irradiation. *Angew Chem, Int Ed Engl*. 2022;61(38), e202207677.
79. Ran L, Li Z, Ran B, et al. Engineering single-atom active sites on covalent organic frameworks for boosting CO_2 photoreduction. *J Am Chem Soc*. 2022;144(37):17097–17109.
80. Yu B, Meng T, Ding X, et al. Hydrogen-bonded organic framework ultrathin nanosheets for efficient visible-light photocatalytic CO_2 reduction. *Angew Chem, Int Ed Engl*. 2022;61(43), e202211482.
81. Pi J, Jia X, Long Z, et al. Surface and defect engineering coupling of halide double perovskite $Cs_2NaBiCl_6$ for efficient CO_2 photoreduction. *Adv Energy Mater*. 2022;12(43), 2202074.
82. Ni B, Zhang G, Wang H, et al. Correlating oxidation state and surface ligand motifs with the selectivity of CO_2 photoreduction to C_2 products. *Angew Chem, Int Ed Engl*. 2023;62(6), e202215574.
83. Pei W, Zhou S, Zhao JJ, et al. Immobilized trimeric metal clusters: a family of the smallest catalysts for selective CO_2 reduction toward multi-carbon products,. *Nano Energy*. 2020;76, 105049.
84. Gong LL, Zhang DT, Shen Y, et al. Enhancing both selectivity and activity of CO_2 conversion by breaking scaling relations with bimetallic active sites anchored in covalent organic frameworks. *J Catal*. 2020;390:126–134.
85. Han ZK, Sarker D, Ouyang R, et al. Single-atom alloy catalysts designed by first-principles calculations and artificial intelligence. *Nat Commun*. 2021;12(1):1833.
86. Zheng X, Ji Y, Tang J, et al. Retracted article: theory-guided Sn/Cu alloying for efficient CO_2 electroreduction at low overpotentials. *Nat Catal*. 2018;2(1):55–61.
87. Herzog A, Bergmann A, Jeon HS, et al. Operando investigation of Ag-decorated Cu_2O nanocube catalysts with enhanced CO_2 electroreduction toward liquid products. *Angew Chem, Int Ed Engl*. 2021;60(13):7426–7435.
88. Shan W, Liu R, Zhao H, et al. In situ surface-enhanced Raman spectroscopic evidence on the origin of selectivity in CO_2 electrocatalytic reduction. *ACS Nano*. 2020;14(9):11363–11372.
89. Chang CJ, Lin SC, Chen HC, et al. Dynamic reoxidation/reduction-driven atomic interdiffusion for highly selective CO_2 reduction toward methane. *J Am Chem Soc*. 2020;142(28):12119–12132.
90. Li YC, Wang Z, Yuan T, et al. Binding site diversity promotes CO_2 electroreduction to ethanol. *J Am Chem Soc*. 2019;141(21):8584–8591.
91. Zhong D, Zhao ZJ, Zhao Q, et al. Coupling of Cu(100) and (110) facets promotes carbon dioxide conversion to hydrocarbons and alcohols. *Angew Chem, Int Ed Engl*. 2021;60(9):4879–4885.
92. Dong H, Zhang L, Li L, et al. Abundant Ce^{3+} ions in $Au-CeO_x$ nanosheets to enhance CO_2 electroreduction performance. *Small*. 2019;15(17), e1900289.
93. Wu X, Zhang W, Li J, et al. Identification of the active sites on metallic MoO_{2-x} nano-sea-urchin for atmospheric CO_2 photoreduction under UV, visible, and near-infrared light illumination. *Angew Chem, Int Ed Engl*. 2023;62(6), e202213124.
94. Chen R, Ren Z, Liang Y, et al. Spatiotemporal imaging of charge transfer in photocatalyst particles. *Nature*. 2022;610(7931):296–301.
95. Xu D, Li K, Jia B, et al. Electrocatalytic CO_2 reduction towards industrial applications. *Carbon Energy*. 2022;(1):5.
96. Jin S, Hao Z, Zhang K, et al. Advances and challenges for the electrochemical reduction of CO_2 to CO: from fundamentals to industrialization. *Angew Chem, Int Ed Engl*. 2021;60(38):20627–20648.
97. Gao J, Li J, Liu Y, et al. Solar reduction of carbon dioxide on copper-tin electrocatalysts with energy conversion efficiency near 20. *Nat Commun*. 2022;13(1):5898.
98. Wang YR, Ding HM, Sun SN, et al. Light, heat and electricity integrated energy conversion system: photothermal-assisted Co-electrolysis of CO_2 and methanol. *Angew Chem, Int Ed Engl*. 2022;61(50), e202212162.

99. Do TN, You C, Kim J. A CO_2 Utilization framework for liquid fuels and chemical production: techno-economic and environmental analysis,. *Energy Environ Sci.* 2022; 15(1):169–184.

100. Lund A, Manohara GV, Song AY, et al. Characterization of chemisorbed species and active adsorption sites in Mg-Al mixed metal oxides for high-temperature CO_2 capture. *Chem Mater.* 2022;34(9):3893–3901.

101. Shao B, Hu GH, Alkebsi KAM, et al. Heterojunction-redox catalysts of $Fe_xCo_yMg_{10}CaO$ for high-temperature CO_2 capture and in situ conversion in the context of green manufacturing. *Energy Environ Sci.* 2021;14(4):2291–2301.

102. Zhu X, Ge T, Yang F, et al. Efficient CO_2 capture from ambient air with amine-functionalized Mg–Al mixed metal oxides. *J Mater Chem.* 2020;8(32):16421–16428.

103. Siegelman RL, Kim EJ, Long JR. Porous materials for carbon dioxide separations. *Nat Mater.* 2021;20(8):1060–1072.

104. Guo Z, Wu H, Chen Y, et al. Missing-linker defects in covalent organic framework membranes for efficient CO_2 separation. *Angew Chem, Int Ed Engl.* 2022;61(41), e202210466.

105. He C, Si DH, Huang YB, et al. A CO_2-masked carbene functionalized covalent organic framework for highly efficient carbon dioxide conversion. *Angew Chem, Int Ed Engl.* 2022;61(40), e202207478.

106. Wang P, Peng Y, Zhu C, et al. Single-phase covalent organic framework staggered stacking nanosheet membrane for CO_2-selective separation. *Angew Chem, Int Ed Engl.* 2021;60(35):19047–19052.

107. Alivand MS, Mazaheri O, Wu Y, et al. Engineered assembly of water-dispersible nanocatalysts enables low-cost and green CO_2 capture. *Nat Commun.* 2022;13(1): 1249.

108. Lin JB, Nguyen TTT, Vaidhyanathan R, et al. A scalable metal-organic framework as a durable physisorbent for carbon dioxide capture,. *Science.* 2021;374(6574): 1464–1469.

109. Zurrer T, Wong K, Horlyck J, et al. Mixed-metal MOF-74 templated catalysts for efficient carbon dioxide capture and methanation. *Adv Funct Mater.* 2020;31(9), 2007624.

110. Algozeeb WA, Savas PE, Yuan Z, et al. Plastic waste product captures carbon dioxide in nanometer pores. *ACS Nano.* 2022;16(5):7284–7290.

111. Seo H, Rahimi M, Hatton TA. Electrochemical carbon dioxide capture and release with a redox-active amine. *J Am Chem Soc.* 2022;144(5):2164–2170.

112. Sullivan I, Goryachev A, Digdaya IA, et al. Coupling electrochemical CO_2 conversion with CO_2 capture. *Nat Catal.* 2021;4(11):952–958.

113. Prajapati A, Sartape R, Galante MT, et al. Fully-integrated electrochemical system that captures CO_2 from flue gas to produce value-added chemicals at ambient conditions. *Energy Environ Sci.* 2022;15(12):5105–5117.

114. Schappi R, Rutz D, Dahler F, et al. Drop-in fuels from sunlight and air. *Nature.* 2022; 601(7891):63–68.

115. Fan JX, Yue XX, Liu YA, et al. An Integration system derived from LDHs for CO_2 direct capture and photocatalytic coupling reaction. *Chem Catal.* 2022;2(3): 531–549.

116. Zheng Y, Chen ZW, Zhang JJ. Solid oxide electrolysis of H_2O and CO_2 to produce hydrogen and low-carbon fuels. *Electrochem Energy Rev.* 2021;4(3):508–517.

117. Li W, Luo JL. High-temperature electrochemical devices based on dense ceramic membranes for CO_2 conversion and utilization. *Electrochem Energy Rev.* 2021;4(3): 518–544.

118. He JF, Li YL, Huang AX, et al. Electrolyzer and catalysts design from carbon dioxide to carbon monoxide electrochemical reduction. *Electrochem Energy Rev.* 2021;4(4): 680–717.

119. Liu B, Wang T, Wang S, et al. Back-illuminated photoelectrochemical flow cell for efficient CO_2 reduction. *Nat Commun.* 2022;13(1):7111.

120. Xie S, Deng C, Huang Q, et al. Facilitated photocatalytic CO_2 reduction in aerobic environment on a copper-porphyrin metal-organic framework. *Angew Chem, Int Ed Engl.* 2023;62(10), e202216717.
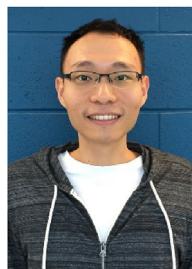
Zhangsen Chen obtained his BS degree at Fuzhou University (2014) and master's degree in physical chemistry from the Research Institute of Photocatalysis, Fuzhou University, in 2017. He is now a Ph.D. student in Prof. Shuhui Sun's group at Institut National de la Recherche Scientifique, Center for Energy, Materials, and Telecommunications (INRS-EMT), Canada. His current research interests focus on the development of advanced nanomaterials and their applications in catalysis and CO_2 conversion to value-added chemicals and fuels.

Gaixia Zhang is a Marcelle-Gauvreau Engineering Research Chair Professor at École de Technologie Supérieure (ÉTS), University of Quebec, Montréal, Canada. She received her Ph.D. degree from Polytechnique Montréal, and then continued her research at Western University and INRS, Canada. Her research interests focus on advanced materials (catalysts, electrodes and electrolytes) for sustainable energy conversion and storage applications, including fuel cells, batteries, hydrogen production, and CO_2 reduction. She is also interested in interface and device engineering, as well as in-situ characterizations and theoretical simulations.

Shuhui Sun is a Full Professor at the Institut National de la Recherche Scientifique (INRS), center for Energy, Materials, and Telecommunications, Canada. He is a Fellow of the Canadian Academy of Engineering (CAE), and a Member of the Royal Society of Canada (RSC College). His current research interests focus on multifunctional nanomaterials for energy conversion and storage applications, including fuel cells, Li-metal batteries, metal-air batteries, Li-/Na-/Zn-ion batteries, H_2 production, and CO_2 reduction. He is the Vice President of the International Academy of Electrochemical Energy Science (IAOEES). He serves as the Executive Editor-in-chief of *Electrochemical Energy Reviews* (EER) and Associate Editor of *SusMat*, as well as the editorial board member of over 10 journals related to nanomaterials and sustainable energy.